Ore Geology Reviews 75 (2016) 252–267

Contents lists available at ScienceDirect

Ore Geology Reviews

journal homepage: www.elsevier.com/locate/oregeorev

Isotopic analysis of the super-large Shuangjianzishan Pb–Zn–Ag deposit in Inner Mongolia, China: Constraints on magmatism, metallogenesis, and tectonic setting

Chunhua Liu [a,*], Leon Bagas [a,b], Fengxiang Wang [a,c]

[a] MLR Key Laboratory of Metallogeny and Mineral Assessment, Institute of Mineral Resources, Chinese Academy of Geological Sciences, 26 Baiwanzhuang Road, Beijing 100037, China
[b] Centre for Exploration Targeting, ARC Centre of Excellence for Core to Crust Fluid Systems, The University of Western Australia, Crawley, WA 6009, Australia
[c] Faculty of Earth Sciences, China University of Geosciences, Wuhan 430074, China

ARTICLE INFO

Article history:
Received 29 September 2015
Received in revised form 18 December 2015
Accepted 21 December 2015
Available online 29 December 2015

Keywords:
Shuangjianzishan
Pb–Zn–Ag deposit
Metallogenesis
Magmatism
Inner Mongolia
Central Asian Orogenic Belt

ABSTRACT

The super-large Shuangjianzishan Pb–Zn–Ag deposit is a newly discovered deposit located in the Huanggang–Ganzhuermiao polymetallic metallogenic belt of Inner Mongolia, NE China. The deposit's resource includes 0.026 Mt Ag, 1.1 Mt Pb, and 3.3 Mt Zn. The deposit is controlled by a NW-trending ductile shear zone and NE- and NW-trending faults in black pelite assigned to the lower Permian Dashizhai Formation. LREE enrichment, HREE depletion, Nb, Ta, P, and Ti depletion, and Zr and Hf enrichment characterize felsic magmatic rocks in the Shuangjianzishan Pb–Zn–Ag district. The ages of porphyritic monzogranite, rhyolitic crystal–vitric ignimbrite, and porphyritic granodiorite are 254–252, 169, and 130 Ma, respectively. Pyrite sampled from the mineralization has Re–Os isochron ages of 165 ± 7 Ma, which suggest the mineralization is associated with the ca. 169 Ma magmatism in the Shuangjianzishan district.

Zircons extracted from the porphyritic granodiorite yield $\varepsilon_{Hf}(t)$ values of −11.34 to −1.41, with t_{DM2} dates of 1275–1901 Ma. The $\varepsilon_{Hf}(t)$ values of zircons in the rhyolitic crystal–vitric ignimbrite and the ore-bearing monzogranite porphyry are 7.57–16.23 and 10.18–15.96, respectively, and their t_{DM2} ages are 177–733 and 257–632 Ma, respectively. Partial melting of depleted mantle resulted in the formation of the ca. 254–252 Ma ore-bearing porphyritic monzogranite and the ca. 169 Ma rhyolitic crystal–vitric ignimbrite; dehydration partial melting of subducted oceanic crust resulted in the formation of the ca. 130 Ma porphyritic granodiorite. The porphyritic monzogranite was emplaced during the late stages of closure of the Paleo-Asian Ocean during the transformation from a collisional to extensional tectonic setting. The ca. 170 and ca. 130 Ma magmatism and mineralization in the Shuangjianzishan district are related to subduction of the Mongolia–Okhotsk Ocean and subduction of the Paleo-Pacific Ocean Plate, respectively.

1. Introduction

The Xing'an–Mongolian Orogenic Belt (XMOB), is an important component of the Central Asian Orogenic Belt (CAOB), and is a Paleozoic tectonic–magmatic belt that was subjected and reworking by Mesozoic tectonic–magmatic activity that formed numbers of ore deposits (Fig. 1a, b) (Chen et al., 2009; Liu and Nie, 2015; Nie et al., 2014, 2015; Wang et al., 2015a; Xu et al., 2013b, 2014, 2015; Zhang et al., 2010b). The Baiyinnuoer–Haobugao mineralization area is situated in the northeastern part of the economically important Huanggang–Ganzhuermiao Fe–Sn–Pb–Zn–Cu–Ag polymetallic metallogenic belt (Fig. 2a), which is located in the southern part of the Great Xing'an Mountains (Fig. 1b; Akiyama and Sun, 2001; Hong et al., 2003; Niu et al., 2006; Ouyang et al., 2014; Shao et al., 1998; Sun and Akiyama, 2001; Wang et al., 2001a, 2008, 2009; Zeng et al., 2009, Zeng et al., 2010a, b, Zeng et al., 2011a, b, Zeng et al., 2012, Zeng et al., 2013a, b; Zhou et al., 2010a, 2011). The Huanggang–Ganzhuermiao belt is 200 km long, 50–55 km wide and trends northeast (Fig. 2a). Economically significant deposits have been discovered within the belt (Table 1).

The newly discovered Shuangjianzishan deposit is located southwest of Ganzhuermiao between the Baiyinnuoer and Haobugao deposits (Fig. 2a). The Shuangjianzishan deposit was discovered by the Second Regional Survey Team of Inner Mongolia during 1984 while mapping the Wuerji 1:50,000-scale sheet area (L–50–131–C). The Third Inner Mongolia Geological Team carried out a mineral reconnaissance survey in the Linba–Fushan area during 1990, although they did not study Shuangjianzishan in detail. Detailed studies of the deposit were conducted in 2004 with drilling during 2004–2006 in the southern part of the area where two small low-grade Pb–Zn occurrences were discovered. The Chifeng Tiantong Geological Exploration Co. Ltd. started detailed 1:10,000-scale geological mapping and prospecting in the

* Corresponding author.
E-mail address: chunhua91052@126.com (C. Liu).

http://dx.doi.org/10.1016/j.oregeorev.2015.12.019
0169-1368/

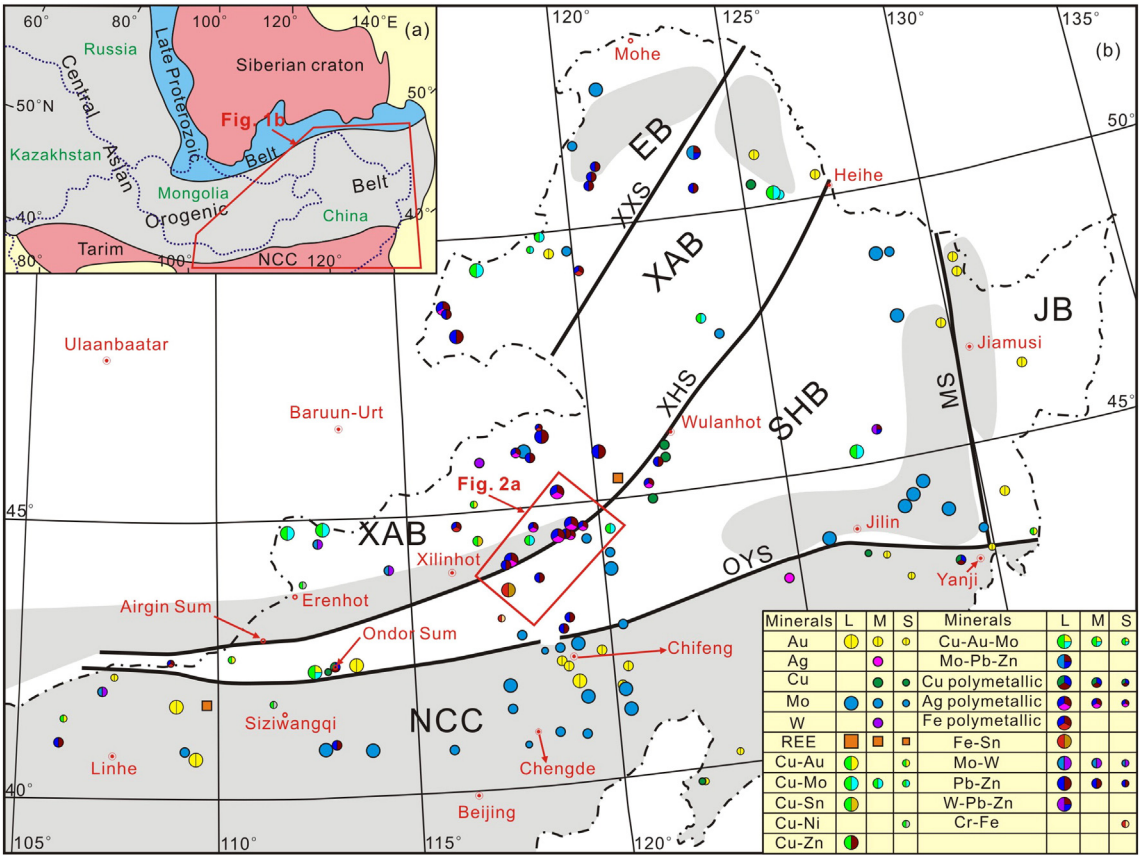

Fig. 1. Location of: (a) the Central Asian Orogenic Belt (modified after Chen et al., 2010); and (b) terranes in the Xing'an–Mongolian Orogenic Belt (XMOB), showing outcrops of Precambrian rocks (modified after Xu et al., 2015) and the distribution of Phanerozoic ore deposits (modified after Liu and Nie (2015) and Zeng et al. (2011a, 2012, 2013a, 2015). EB: Erguna Block; XAB: Xing'an–Airgin Sum Block; SHB: Songliao–Hunshandake Block; JB: Jiamusi Block; XXS: Xinlin–Xiguitu Suture; XHS: Xilinhot–Heihe Suture; MS: Mudanjiang Suture; OYS: Ondor Sum–Yanji Suture.

broader Shuangjianzishan area during 2007, and the company delineated mineralized and altered outcrop in a small area in the eastern Xinglongshan part of the district. The company consequently began a 1:10,000 geophysical IP surveys that delineated 10 geophysical anomalies, which lead to the drilling and discovery of Ag-bearing polymetallic orebodies (Sun et al., 2010). By 2010, 46 orebodies were discovered and evaluated, and the resources of 21 orebodies were estimated to contain 181 Mt ore, including 0.026 Mt Ag, 1.1 Mt Pb, and 3.3 Mt Zn (Sun et al., 2010). It is now recognized that this is the site of a super-large Pb–Zn–Ag polymetallic district. With further prospecting and evaluation, it is expected that the measured size of the deposit will increase significantly.

Wu et al. (2014) studied the occurrences of silver in the Shuangjianzishan Pb–Zn–Ag deposit. Within the ore district, the relationship between the Pb–Zn–Ag polymetallic mineralization and the magmatism remain unclear. The age, origin, and evolution of the magmatic activity, and the relationship between the magma and metallogenic fluids are critical for understanding the origin of the deposits and their geodynamic setting. Therefore, in this study we conducted systematic petrographic research on the magmatic rocks in the Shuangjianzishan Pb–Zn–Ag deposit to constrain the ages of magmatism and the origins of the magma by completing whole-rock geochemical analyses, zircon laser ablation-inductively coupled plasma-mass spectrometry (LA-ICP-MS) geochronology, and analyses of zircon Hf isotopes. We report on the Re–Os isochron age of pyrite to constraint the age of mineralization at the Shuangjianzishan Pb–Zn–Ag deposit. Finally, we propose a relationship between the magmatism and the Shuangjianzishan Pb–Zn–Ag polymetallic mineralization using detailed geochronology.

2. Regional geological setting

2.1. Regional tectonic evolution

The CAOB is one of the most remarkable global example of accretion and transformation of crustal terranes (Windley et al., 2007; Wu et al., 2011; Xiao and Santosh, 2014; Xiao et al., 2003; Zeng et al., 2012, 2014a). The crustal evolution over the past billion years bears witness to continental margin accretion, and post-collision and intracontinental orogenies accompanied by the strong interaction between crust and the mantle (Xiao et al., 2003).

The southern part of the Great Xing'an Mountains is located in the eastern part of Inner Mongolia, and is part the XMOB in the eastern portion of the CAOB between the Siberian Plate and North China Craton (NCC; Bai et al., 2014). Xu et al. (2014, 2015) proposed an updated division scheme for the XMOB, in which pre-Middle Devonian (>400 Ma) tectonic units are divided into an orogenic belt with four blocks separated by crustal sutures (Fig. 1b). The Huanggang–Ganzhuermiao polymetallic metallogenic belt is situated in the western section of the Xilinhot–Heihe Suture (XHS) (Fig. 1b).

The tectonic evolution of the Paleo-Asian Ocean is characterized by bi-directional subduction along the active southern margin of the Siberia Craton and the northern margins of the NCC and Tarim Craton (Fig. 1b; Chen et al., 2009; Jian et al., 2008; Li et al., 2011, 2015; Xiao et al., 2003, 2008, 2009; Xiao and Santosh, 2014; Xu et al., 2013a; Zhang et al., 2009d). It is generally accepted that closure of the Paleo-Asian Ocean took place along the Solonker Suture (Cao et al., 2013; Chen et al., 2015; Cheng et al., 2014; Hu et al., 2015; Jian et al., 2008, 2010; Li et al., 2013, 2014; Liu et al., 2013; Wang et al., 2013, 2015b;

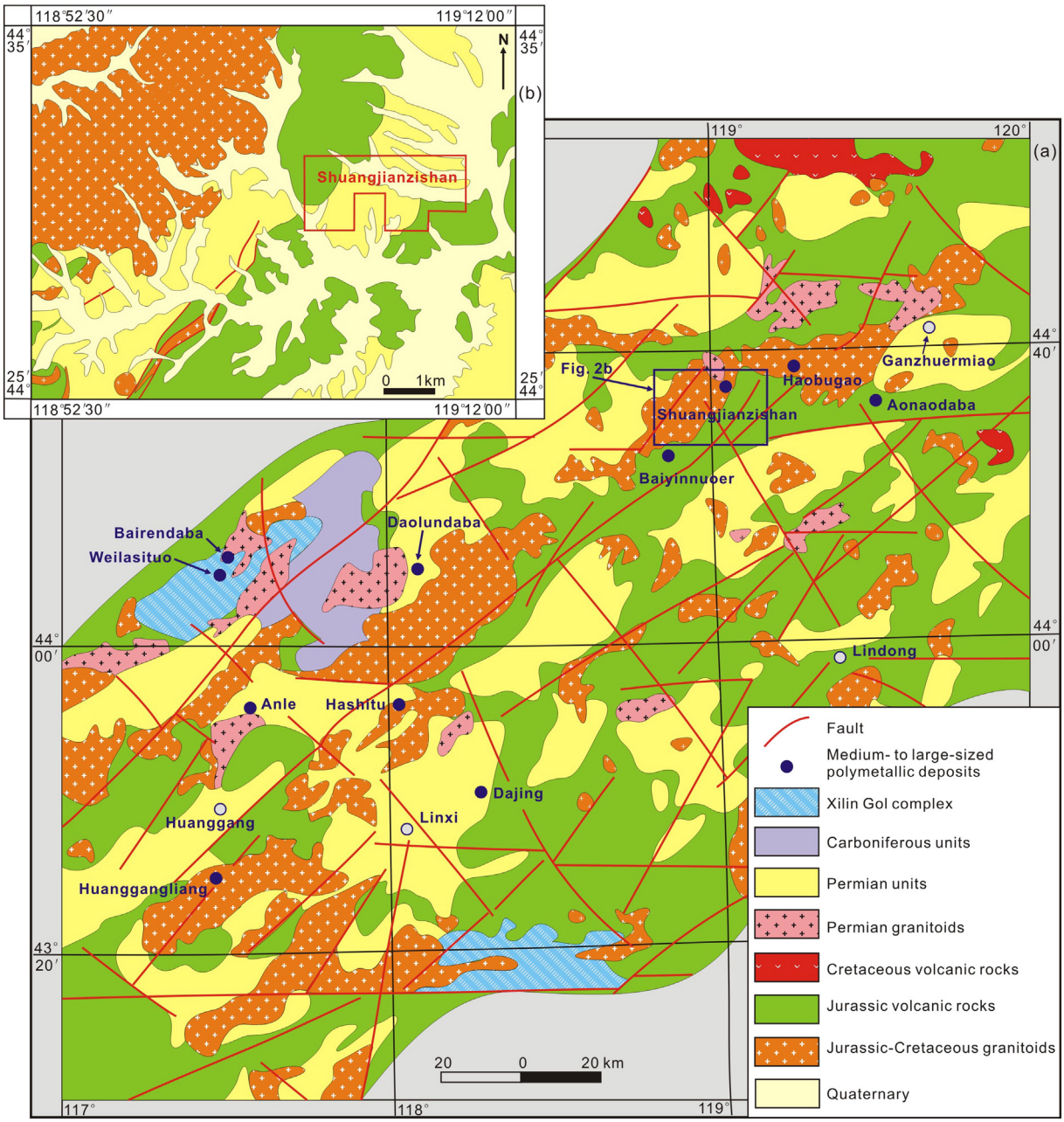

Fig. 2. Geological maps of: (a) the Huanggang–Ganzhuermiao metallogenic belt, Inner Mongolia (modified after Wang et al., 2001a); and (b) the Shuangjianzishan Pb–Zn–Ag deposit (modified after Sun et al., 2010).

Wu et al., 2011; Xu et al., 2015; Zhang et al., 2007, 2009b, 2012b, 2013c, 2014). Tong et al. (2015) summarized previous estimates of the timing of closure of the Paleo-Asian Ocean, which are ca. 420–400 Ma, 370–350 Ma, ~260 Ma, and 250–240 Ma, and they proposed a new estimate of >285–275 Ma.

The Great Xing'an Mountains became a part of the circum-Pacific continental margin of the Eurasian Plate during the Jurassic. As a result of NNW-directed subduction of the Pacific Plate, this region gradually became uplifted, resulting in the development and reactivation of faults. With closure of the Mongolia–Okhotsk Ocean and increased compression between the Eurasian and Pacific plates during the Late Jurassic, new NE-trending active belts developed. These belts are characterized by zones of uplift and depression accompanied by large-scale volcanic eruptions and magmatic intrusions, so that together they form an important Mesozoic NE-trending tectono-magmatic belt (Zhao and Zhang, 1997; Sheng and Fu, 1999).

Northeast-trending faults in the Huanggang–Ganzhuermiao metallogenic belt are common throughout the area, with the longest being >100 km in length. These faults intersect NW-trending faults forming a lattice-type arrangement, and they are closely associated with folds of various periods, providing structures that host mineral resources (Fig. 2a; Zhang and Zhang, 2003).

2.2. Regional stratigraphic sequence

Permian and Jurassic units are exposed in the Baiyinnuoer–Haobugao metallogenic belt (Fig. 2a). A widespread Permian succession of sedimentary and volcanic rocks makes up much of the Great Xing'an Mountains. Both Early and Late Permian strata form the main part of the NE-trending Huanggangliang Anticlinorium in the study area. The Early Permian units are, from oldest to youngest, the Qingfengshan, Dashizhai, and Huanggangliang formations, which are unconformably

Table 1
Ages of felsic intrusives and economically significant deposits in the Huanggang–Ganzhuermiao metallogenic belt.

Deposits	Sample details	Methods	Ages (Ma)	References
Huanggangliang Sn–Fe	Granite	Zircon LA-ICP-MS U–Pb	139.96 ± 0.87 (a)	Zhai et al. (2014b)
	Molybdenite	Re–Os isochron	134.9 ± 5.2 (b)	Zhai et al. (2014b)
	Granite	Zircon LA-ICP-MS U–Pb	140 ± 1 (a)	Zhai et al. (2012)
	Molybdenite	Re–Os isochron	135 ± 5 (b)	Zhai et al. (2012)
	"204" granite	Rb–Sr isochron	142.05 (a)	Zhao and Zhang, (1997)
	Amphibole in skarn	K–Ar	140 (b)	Wang et al. (2001a)
	Amphibole in skarn	K–Ar	130 ± 3 (b)	Wang et al. (2001b)
	Muscovite in aplite	K–Ar	142 ± 3(b)	Ishiyama et al. (2001)
	K-feldspar in aplite	K–Ar	131 ± 3 (b)	Ishiyama et al. (2001)
	K-feldspar in tin vein	K–Ar	137 ± 3 (b)	Ishiyama et al. (2001)
Baiyinnuoer Pb–Zn–Ag	Dioritic porphyrite	Zircon LA-ICP-MS U–Pb	242.3 ± 3.6 (a, b)	Yi et al. (2012)
	Quartz monzonite	Zircon LA-ICP-MS U–Pb	243.0 ± 1.4 (a, b)	Yi et al. (2012)
	Biotite syenogranite	Zircon LA-ICP-MS U–Pb	134.8 ± 1.2 (a)	Jiang et al. (2011)
	Quartz porphyry	Zircon LA-ICP-MS U–Pb	129.2 ± 1.4 (a)	Jiang et al. (2011)
	Granodiorite	Zircon LA-ICP-MS U–Pb	244.5 ± 0.9 (a, b)	Jiang et al. (2011)
	Andesite	Zircon LA-ICP-MS U–Pb	135 (a)	Jiang et al. (2011)
Haobugao Sn–Fe–Pb–Zn–Cu–Ag	Ulan Dam biotite granite	Rb–Sr isochron	132.2 (b)	Zhang and Zhao, (1993)
	Syenogranite	Rb–Sr isochron	131 (b)	Zhang and Zhao, (1993)
Dajing Cu–Sn–Ag	Felsite dyke inside the ore district	Zircon LA-ICP-MS U–Pb	170.7 ± 1.4 (a)	Jiang et al. (2012)
	Felsite dyke inside the ore district	Zircon LA-ICP-MS U–Pb	170.7 ± 1.1 (a)	Jiang et al. (2012)
	Biotite monzonitic granite outside the ore district	Zircon LA-ICP-MS U–Pb	279.7 ± 1.3 (a)	Jiang et al. (2012)
	Andesitic porphyrite dyke outside the ore district	Zircon LA-ICP-MS U–Pb	252.0 ± 1.8 (a)	Jiang et al. (2012)
	Biotite monzonitic granite outside the ore district	Zircon LA-ICP-MS U–Pb	242.8 ± 1.7 (a)	Jiang et al. (2012)
	Rhyolitic volcanic rock outside the ore district	Zircon LA-ICP-MS U–Pb	143–146 (a)	Jiang et al. (2012)
	Quartz porphyry dyke outside the ore district	Zircon LA-ICP-MS U–Pb	146.1 ± 0.9 (a)	Jiang et al. (2012)
	Andesite porphyry outside the ore district	Zircon LA-ICP-MS U–Pb	133.2 ± 0.7 (b)	Jiang et al. (2012)
	Altered dacite porphyry	K–Ar	132.8 (b)	Wang et al. (2001a)
	Altered sericite near ore vein	^{40}Ar–^{39}Ar	138.3 (b)	Wang et al. (2001a)
Anle Sn–Cu–Zn	Granite porphyry	Rb–Sr isochron	134.2 (a)	Wang, (1997)
	K-feldspar in concealed granite	K–Ar	132 ± 3 (a)	Ishiyama et al. (2001)
	Sericite in quartz sericite vein	K–Ar	133 ± 3 (b)	Ishiyama et al. (2001)
Bairendaba Ag–Pb–Zn	Granodiorite	Zircon SHRIMP U–Pb	319 ± 3 (a)	Xue et al. (2010)
	Diorite	Zircon SHRIMP U–Pb	326.5 ± 1.6 (a)	Liu et al. (2010)
	Muscovite	^{40}Ar–^{39}Ar	135.0 ± 3 (b)	Chang and Lai, (2010)
Weilasituo Sn–Cu–Ag	Muscovite	^{40}Ar–^{39}Ar	133.4 ± 0.8 (b)	Pan et al. (2009)
	Diorite	Zircon SHRIMP U–Pb	310 ± 2 (a)	Xue et al. (2010)
	Quartz diorite	Zircon SHRIMP U–Pb	311 ± 2 (a)	Xue et al. (2010)
Daolundaba Cu–W	Biotite granite	Zircon LA-ICP-MS U–Pb	292.1 ± 0.84 (a)	Zhou et al. (2014)
	Dacitic crystal tuff	Zircon SHRIMP U–Pb	300 ± 5 (a)	Xue et al. (2010)
Hashitu Mo	Granite	Zircon LA-ICP-MS U–Pb	147 ± 1 (a)	Zhai et al. (2014a)
	Granite porphyry	Zircon LA-ICP-MS U–Pb	143 ± 2 (a)	Zhai et al. (2014a)
	Granite porphyry	Zircon LA-ICP-MS U–Pb	149.5 ± 1 (a, b)	Zeng et al. (2012)
	Molybdenite	Re–Os isochron	150 ± 4 (b)	Pan et al. (2009)
	Molybdenite	Re–Os isochron	148.8 (b)	Zhang et al. (2012a)
Aonaodaba Sn–Cu–Ag	Granite porphyry	Rb–Sr isochron	148 (a, b)	Zhao et al. (1994)
Shuangjianzishan Pb–Zn–Ag	Quartz porphyry	Zircon LA-ICP-MS U–Pb	239.08 ± 0.94 (a)	Wu et al. (2013)
	Sphalerite	Rb–Sr isochron	132.7 ± 3.9 (b)	Wu et al. (2013)
	Pyrite	Re–Os isochron	165 ± 7.1 (b)	This study
	Rhyolitic crystal–vitric ignimbrite	Zircon LA-ICP-MS U–Pb	169 ± 3.4 (a)	This study
	Porphyritic granodiorite	Zircon LA-ICP-MS U–Pb	130 ± 5.6 (a)	This study
	Ore-bearing porphyritic monzogranite	Zircon LA-ICP-MS U–Pb	254 ± 3 (a)	This study
	Ore-bearing porphyritic monzogranite	Zircon LA-ICP-MS U–Pb	252 ± 3.2 (a)	This study

(a) Magmatic ages; (b) metallogenic ages.

overlain by the Late Permian Linxi Formation. The Dashizhai Formation is extensively distributed, and is exposed symmetrically on both flanks of the Huanggangliang Anticlinorium. The Huanggangliang Formation is also exposed symmetrically on both flanks of the anticlinorium and forms NE-trending zones that conformably overlap the Dashizai Formation (Zhou et al., 2010b). Jurassic units in the region are divided into the Hongqi Formation at the base succeeded by the Wanbao, Xinmin, and Manketou'ebo formations (Shao, 2007).

2.3. Regional magmatism and metallogenesis

The southern Great Xing'an Mountains records five periods of magmatism (326–301, 287–251, 248–216, 182–160, and 146–119 Ma; Ouyang, 2013). The intrusive activity peaked in the Late Mesozoic (ca. 155–120 Ma) simultaneously with large-scale mineralization (Ouyang et al., 2014).

3. Geology of the Shuangjianzishan Pb–Zn–Ag deposit

3.1. Stratigraphy

The stratigraphic units in the Shangjianzishan area include the Early Permian Dashizhai, Middle Jurassic Xinmin and Late Jurassic Manketou'ebo formations, and unassigned Holocene sediments (Fig. 2b). The lower part of the Dashizhai Formation consists of an altered succession of grayish-green andesite with pillow structures, and andesitic tuff intercalated with dark-gray pelite. The upper part of the formation consists of thickly bedded metasiltstone and dark-gray pelite.

The Xinmin Formation unconformably overlies the Dashizhai Formation outcropping in the southeastern part of the region. The lower part of the Xinmin Formation consists of sandy conglomerate and siltstone intercalated with carbonaceous mudstone and thin coal seams. The upper part of the formation consists of rhyolitic tuff and rhyolitic ignimbrite.

The Manketou'ebo Formation unconformably overlies the Dashizhai Formation and consists of tuffaceous sandstone and rhyolitic tuff.

3.2. Structure

A NW-trending ductile shear zone and NE- and NW-trending faults are the main structures in the district. The shear zone is developed in the central and eastern parts of the district and is hosted by black, pelite assigned to the Dashizhai Formation. The shear zone is 1000–1400 m wide, more than 4000 m long, and generally strikes NW dipping 55°–65° SW (Fig. 3). The NE-trending faults strike 020°–040° and dip ~60° NW. The faults are generally 1–8 m wide and 50–600 m long, and control the distribution of the NE-trending Ag polymetallic deposits in the district (Sun et al., 2010). The NW-trending faults strike typically dip 45°–65° NE, and are coeval with the NE-trending faults. The NW-faults are 6–15 m wide, >400 m long, and compressive fractures containing quartz–sulfide veins are developed along the edges of the faults (Sun et al., 2010). The NE- and NW-trending faults appear to form a conjugate set that are associated with the development of the caldera formed by the Shuangjianzishan volcano (Sun et al., 2010).

3.3. Magmatic rocks

A suite of felsic magmatic rocks is present in the ore district, as determined by drill hole exploration (Fig 4). The suite includes porphyritic granodiorite and porphyritic monzogranite, and volcanic rocks include rhyolitic tuff and ignimbrite. The orebodies are hosted mainly in pelite, as well as in porphyritic monzogranite (Fig. 3).

3.4. Occurrence of the orebodies

The orebodies have been comprehensively described in Sun et al. (2010). The Shuangjianzishan deposit includes two distinct orebodies located ~5 km apart. The deposit to the west is known as the Shuangjianzishan ore area and the one to the east is the Xinglongshan ore area. The Shuangjianzishan ore area is the smaller of the two and requires less engineering work to mine, while the Xinglongshan ore area contains more mineralization, but requires more engineering work to mine. Based on the trend of the orebodies and their metallogenic sequences, it is possible to distinguish an Ag-polymetallic lode hosted by a NW-trending shear zone in the central-eastern part of the district from a series of NE- and NW-trending Ag polymetallic orebodies, which fill the circular and radial fractures surrounding the Shuangjianzishan caldera (Sun et al., 2010).

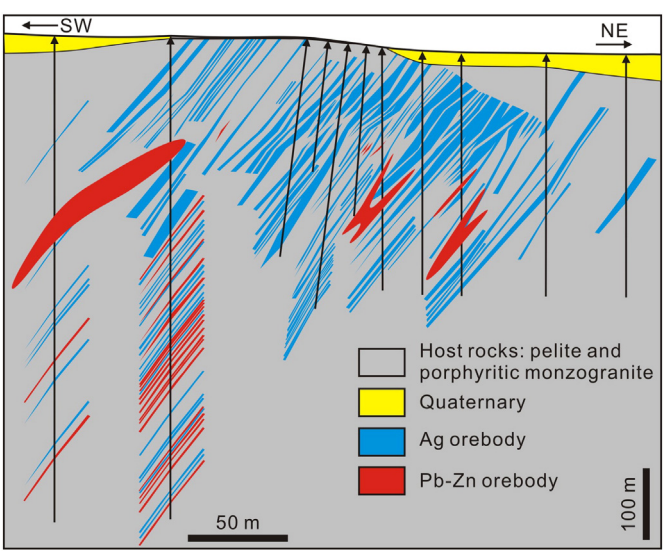

Fig. 3. Simplified geological map of the Shuangjianzishan Pb–Zn–Ag deposit showing the distribution of orebodies and the spatial relationship between orebodies and pelite and porphyritic monzogranite (modified after Sun et al., 2010).

The NW-trending Ag polymetallic lode dips 50°–65° SW in a mineralized area that is >2000 m long and ~1200 m wide. More than 100 densely packed, parallel Ag polymetallic veins have been identified in the lode with drilling and tunneling (Fig. 3; Sun et al., 2010). The Pb–Zn–Ag polymetallic orebodies form as veins and lenses, with single lodes being 100–800 m long, and commonly 1–10 m wide with a maximum thickness of ~100 m. The mineralization consists of pyrite and sphalerite with minor amounts of galena. The sulfides in the orebodies are disseminated or form stockworks with an average grade of 98 g/t Ag, 1.6 wt.% Zn, and 0.6 wt.% Pb. Alteration associated with the mineralized is characterized by chlorite (Sun et al., 2010).

Drilling has outlined the distribution of Ag–Cu polymetallic orebodies at Shuangjianzishan, which are situated in the hanging wall of the shear zone, and are more than 300 m long and up to 3 m thick. The mineralization consists of chalcopyrite, sphalerite, pyrite, and minor amounts of galena. The average grade of this style of mineralization is 0.65 wt.% Cu, 264 g/t Ag, 2.15 wt.% Zn, and 0.86 wt.% Pb.

The NE-trending orebodies are distributed in the central-eastern part of the mining area. Five parallel orebodies have delineated during mining underground. The orebodies generally strike 020°–030°, dip >65° NW, are >600 m long, and up to 6 m thick. The mineralization consists of quartz veins containing sphalerite, galena, and pyrite. Its average grade is >400 g/t Ag, 2.5 wt.% Zn and 3.2 wt.% Pb, and the alteration is characterized by chlorite and silica (Sun et al., 2010).

The NW-trending orebodies are >400 m long, up to 15 m thick, and consist of sphalerite–galena–pyrite forming irregular vein and disseminations (Fig. 3). Their average grade is ~400 g/t Ag (with a maximum of >10,000 g/t), 2.8 wt.% Zn, and 4.3 wt.% Pb. Alteration associated is characterized predominantly by chlorite and silica followed by pyrophyllitic and kaolinitic alteration (Sun et al., 2010).

3.5. Ore mineralogy

Ore minerals at Shuangjianzishan include sphalerite, galena, pyrite, marcasite, and small amounts of limonite (Fig. 5). Silver-bearing minerals include polybasite, canfieldite, aguilarite, pyrargyrite, freibergite, argentite, kustelite, and native silver (Wu et al., 2014). Four stages of mineralization have been recognized in the area progressing from: (1) quartz and sphalerite; (2) galena, sphalerite, and silver minerals; (3) quartz and silver minerals; to (4) pyrite and carbonate. Most of the silver minerals were deposited during the second and third stages (Wu et al., 2014). The gangue minerals include quartz, chlorite, calcite, epidote, and pyrophyllite (Sun et al., 2010).

4. Sampling and analytical methods

We collected and analyzed the felsic magmatic rocks (i.e. rhyolitic ignimbrite, porphyritic granodiorite and porphyritic monzogranite; Fig. 4a–d) and pyrite (Fig. 5) from the drill holes and ore heap at the Shuangjianzishan Pb–Zn–Ag deposit. The petrographic characteristics of the felsic magmatic rocks are described below.

4.1. Petrography of magmatic rocks

The rhyolitic ignimbrite is light red, pyroclastic, and has pseudofluidal structures (Fig. 4a). The tephra is mainly quartz, plagioclase, K-feldspar, and vitric fragments, with minor detritus. The quartz fragments are generally show resorption texture.

The porphyritic granodiorite is pale in color (Fig. 4c), while the altered porphyritic granodiorite is light red in color (Fig. 4b). Phenocrysts (~30 vol.%) in the porphyritic granodiorite are plagioclase and K-feldspar with minor quartz. The matrix consists of quartz (~30 vol.%), plagioclase (~20 vol.%), K-feldspar (~10 vol.%), biotite

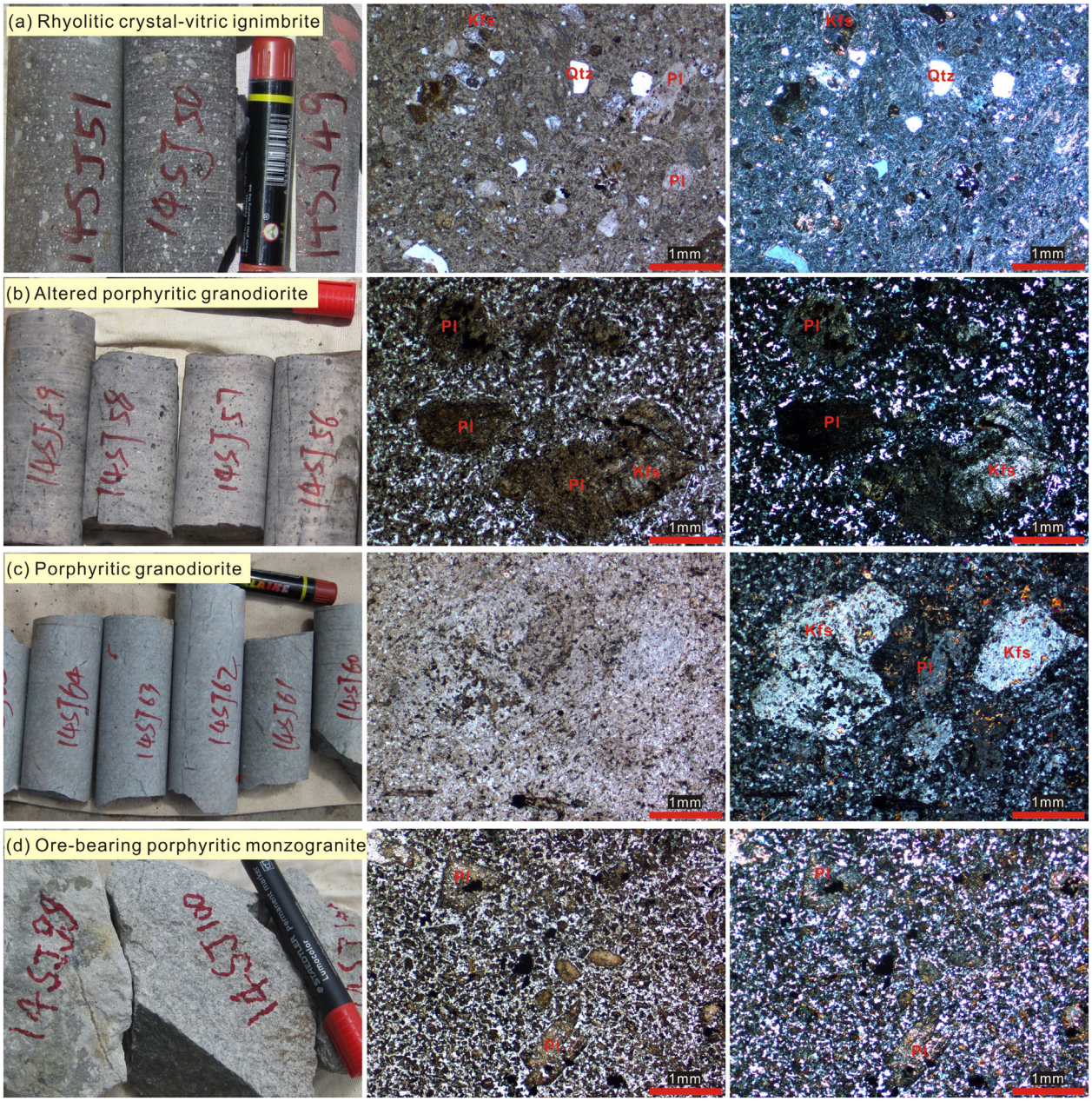

Fig. 4. Magmatic rocks at the Shuangjianzishan Pb–Zn–Ag deposit, shown in hand specimen photographs and thin section photomicrographs under plane polarized light and cross-polarized light for each sample. Kfs: K-feldspar; Pl: plagioclase; Qtz: quartz.

(~8 vol.%), and accessory minerals (~2 vol.%) include zircon and apatite. The plagioclase is partially altered to sericite and kaolin (Fig. 4b).

The porphyritic monzogranite is gray containing phenocrysts of plagioclase (~20 vol.%) and minor K-feldspar (Fig. 4d). The matrix consists of quartz (~30 vol.%), plagioclase (~10 vol.%), K-feldspar (~30 vol.%), biotite (~8 vol.%), and accessory minerals (~2 vol.%) of zircon and apatite. The plagioclase has been partially altered to sericite and carbonate minerals.

4.2. Analytical methods

Zircons were separated from the samples using standard techniques of density and magnetic separation at the Institute of Regional Geology and Resource Surveys, Langfang, Hebei Province, China. Transmitted-light and reflected-light images were obtained using an optical microscope. Cathodoluminescence (CL) images of the zircon grains were obtained prior to analysis using a scanning electron microscope (SEM) at the SEM Laboratory of Peking University in Beijing, China. In situ U–Pb zircon dating was conducted using a LA-ICP-MS (ELAN DRC-II) at the Key Laboratory of Crust–Mantle Materials and Environments, University of Science and Technology of China, Chinese Academy of Sciences, Anhui Province, China. Laser ablation spot diameters ranged from 40 to 32 μm, and samples were ablated to depths of 20–40 μm. The carrier gas was He and an external zircon standard (91500) was analyzed after every four sample points. The NIST SRM610 standard was used for calibrating element concentrations. The U–Pb ratio data were processed using the LaDating@Zrn Excel VBA program, and ComPb corr#3-18 (Andersen, 2002) was used for Pb isotopic correction. Isoplot (ver. 3.0) was used to calculate weighted mean ages and generate concordia plots (Ludwig, 2003).

Five ore samples were selected from Shuangjianzishan for pyrite Re–Os dating, all of which were fresh samples collected from the mine. Gravitational and magnetic separation techniques were applied and then handpicked under a binocular microscope. Re–Os isotopic

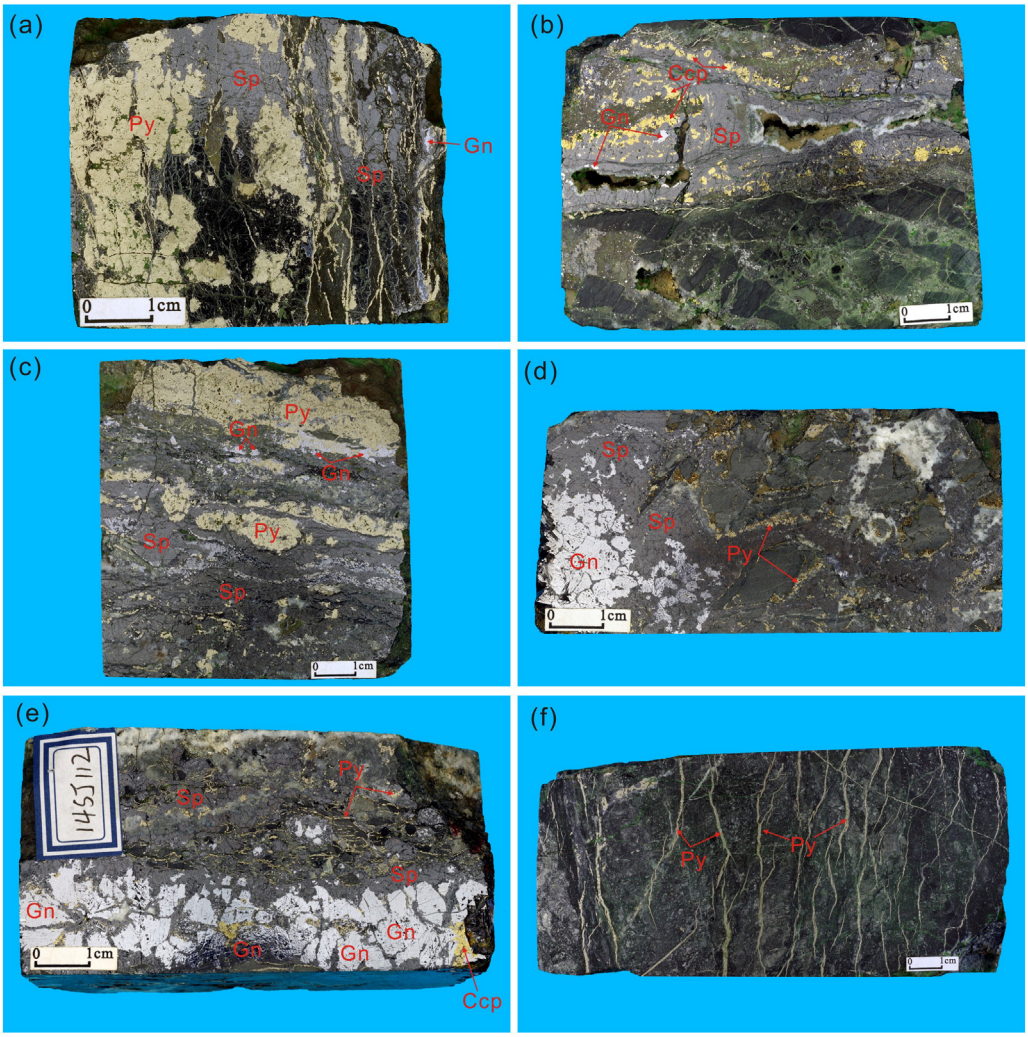

Fig. 5. Photographs of hand specimens showing mineral paragenesis in various ore stages at the Shuangjianzishan Pb–Zn–Ag deposit. Py: pyrite; Gn: galena; Sp: sphalerite; Ccp: chalcopyrite.

analyses were performed at the National Research Center of Geoanalysis, Chinese Academy of Geosciences. The instrument used is an ICP-MS (TJA X-series), made by Thermo Electron Corporation in the USA. The details of the chemical procedure have been described by Du et al. (1995, 2001, 2004); Shirey and Walker (1995); Stein et al. (1998) and Markey et al. (1998).

Rock samples were sawed into small chips, ultrasonically cleaned in distilled water with <3% HNO_3 and then in distilled water and subsequently dried and handpicked to remove visible contamination. The rocks were crushed and ground in a tungsten-carbide ring mill, and the resulting powder was used for analyses of major and trace elements at the Hebei Institute of Regional Geological and Mineral Resource Survey at Langfang in the Hebei Province of China. Major elements were analyzed using X-ray fluorescence (XRF) spectrometry with analytical uncertainties <5%. Trace and rare earth elements were analyzed using an inductively coupled plasma mass spectrometry (ICP-MS). Analytical uncertainties are 10% for elements with abundances <10 ppm, and around 5% for those >10 ppm.

Zircon Hf isotope analyses were conducted in situ using a New Wave UP213 laser-ablation microprobe attached to a Neptune multi-collector ICP-MS at the Institute of Geology, Chinese Academy of Geological Sciences in Beijing. Instrumental conditions and data acquisition protocols are comprehensively described in Hou et al. (2007) and Wu et al. (2006). A stationary spot was used for analyses. The beam diameter was 44 μm, and helium was used as the carrier gas to transport ablated sample from the laser ablation cell to the ICP-MS torch via a mixing chamber containing argon. Zircon GJ1 was used as a standard reference material during routine analyses; its weighted mean $^{176}Hf/^{177}Hf$ ratio of 0.282001 (2σ, n = 11) is indistinguishable from that obtained in the in situ analysis conducted by Elhlou et al. (2006) ($^{176}Hf/^{177}Hf = 0.282015 \pm 19$; 2σ).

5. Analytical results

5.1. Zircon U–Pb dating

The CL images of the zircon grains analyzed are included in Fig. 6, and Fig. 7 shows zircon U–Pb concordia diagrams; the age data are presented in Appendix A.1.

The Th/U ratios of the zircons from the rhyolitic crystal–vitric ignimbrite (Sample 14SJ53) are 0.43–0.82 (Appendix A.1), and 52 spots were analyzed yielding a weighted mean $^{206}Pb/^{238}U$ age of 169 ± 3 Ma (MSWD = 0.09, n = 37) (Fig. 7a).

The Th/U ratios for the zircons from Sample 14SJ55 of porphyritic granodiorite are 0.51–1.43 (Appendix A.1). A total of 28 spots were analyzed yielding a weighted mean $^{206}Pb/^{238}U$ age of 130 ± 6 Ma (MSWD = 0.19, n = 14) (Fig. 7b).

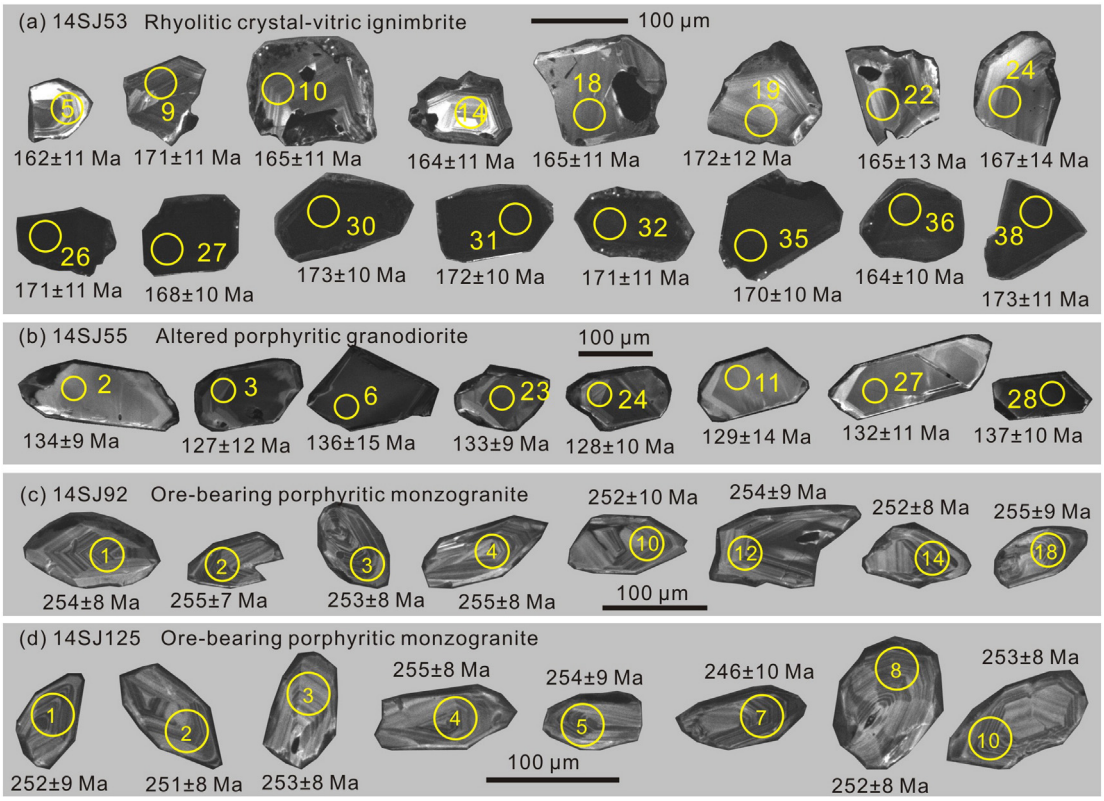

Fig. 6. Cathodoluminescence images of zircons from felsic magmatic rocks at the Shuangjianzishan Pb–Zn–Ag deposit. Yellow circles indicate the locations of U–Pb dating analyses. (For interpretation of the references to color in this figure legend, the reader is referred to the web version of this article.)

The Th/U ratios for zircons from Samples 14SJ92 and 14SJ125 of the porphyritic monzogranite are 0.39–1.14 and 0.41–0.86 (Appendix A.1). A total of 30 spots were analyzed from each of the samples yielding weighted mean $^{206}Pb/^{238}U$ ages of 254 ± 3 Ma (MSWD = 0.05, n = 28) and 252 ± 3 Ma (MSWD = 0.06, n = 28) (Fig. 7c–d). The $^{207}Pb/^{235}U$ in the diagrams 7b to 7d drift to the right because of the ^{207}Pb gain and ^{206}Pb loss in the samples of 14SJ55, 14SJ92, and 14SJ125 (Fig. 7b–d).

5.2. Pyrite Re–Os dating

The concentrations of Re and Os and the Os isotopic compositions of pyrite from the area around Shuangjianzishan are shown in Table 2. The total Re, common Os, and ^{187}Os concentrations of the Shuangjianzishan pyrite are 0.0215–0.0854 ng/g, 0.0029–0.0227 ng/g, and 0.000368–0.002364 ng/g, respectively. The data of 14SJ19 and 14SJ101 have been eliminated because the existence of rhenium gain and/or osmium loss (Fig. 8a). The data of samples 14SJ16, 14SJ99, and 14SJ106, processed using the Isoplot (ver. 3.0) program (Ludwig, 2003), yielded an isochron age of 165 ± 7 Ma with a MSWD = 0.68 and an initial $^{187}Os/^{188}Os$ of 0.7895 ± 0.0029 (Fig. 8b). The isochron age is interpreted as an age of the Pb–Zn–Ag mineralization in the Shuangjianzishan deposit.

5.3. Whole-rock major and trace element compositions

Table 3 lists the whole-rock geochemical data for the felsic magmatic rocks from the Shuangjianzishan Pb–Zn–Ag deposit. Fig. 9 presents the Q–A–P, SiO_2–K_2O, and A/CNK–A/NK diagrams, and Fig. 10 shows the REE chondrite-normalized diagrams and primitive-mantle-normalized trace element spider diagrams.

5.3.1. Major elements

Most of the ore-bearing porphyritic monzogranite and rhyolitic crystal–vitric ignimbrite samples plot in the high-K calc-alkaline field, while all the porphyritic granodiorite plot in the calc-alkaline and shoshonite fields on the SiO_2–K_2O diagram (Fig. 9b). All samples plot in the peraluminous field on an A/CNK–A/NK diagram (Fig. 9c). The A/CNK and A/NK values for the rhyolitic crystal–vitric ignimbrite are in the range of 1.99–2.07 and 2.07–2.17, respectively. Those of the ore-bearing porphyritic monzogranite are 1.56–1.83 and 1.62–1.91, and those of the porphyritic granodiorite are 1.19–1.21 and 1.36–1.38 (Table 3). The A/CNK and A/NK values for the rhyolitic crystal–vitric ignimbrite and the ore-bearing porphyritic monzogranite are higher than those of the other rocks.

5.3.2. Trace elements

The REE chondrite-normalized diagrams for the porphyritic granodiorite, and ore-bearing porphyritic monzogranite are similar being right-inclined with strongly fractionated LREEs and HREEs, and weak negative δEu anomalies (Fig. 10a). The porphyritic granodiorite yields δEu values of 0.8–1.02, LREE/HREE values of 11.81–12.75, and La_N/Yb_N values of 17.43–21.55. The ore-bearing monzogranite porphyry has δEu values of 0.69–0.77, LREE/HREE values of 9.13–13.12, and La_N/Yb_N values of 10.9–19.88. The rhyolitic crystal–vitric ignimbrite has a δEu value of 0.05, LREE/HREE values of 3.96–4.2, and La_N/Yb_N values of 2.74–3.16, and right-type "seagull" patterns, and moderate fractionation of LREEs and HREEs (Fig. 10a).

Spider diagrams for the rocks in the ore district are similar to one another and also differ significantly in part (Fig. 10b). The rhyolitic crystal–vitric ignimbrite, porphyritic granodiorite, and ore-bearing porphyritic monzogranite are relatively depleted in Nb, Ta, P, and Ti, and relatively enriched in Zr and Hf. The Sr and Sr/Y values for the units are shown in Table 4.

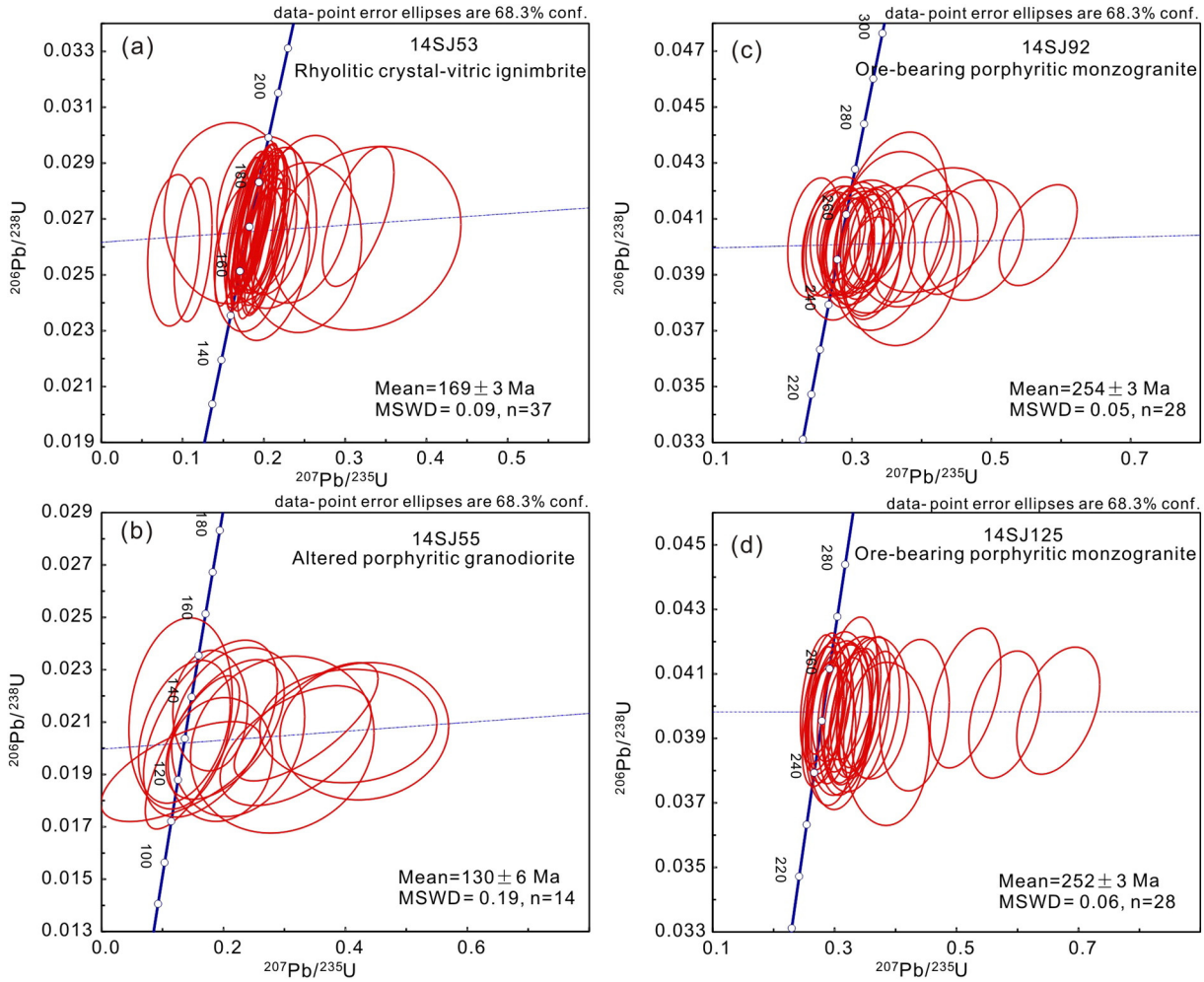

Fig. 7. $^{206}Pb/^{238}U$ versus $^{207}Pb/^{235}U$ concordia diagrams for felsic magmatic rocks at the Shuangjianzishan Pb–Zn–Ag deposit.

As can be seen from Table 4, the Sr and Sr/Y values for the porphyritic granodiorite are significantly higher than those of the other rocks. The values for Ag, Pb, and Zn are shown in Table 3 for each of the felsic units.

5.4. Zircon Hf isotope results

The zircon $^{206}Pb/^{238}U$ versus $\varepsilon_{Hf}(t)$ diagrams are shown in Fig. 11 and the isotopic data for zircon Hf isotope analyses are presented in Table 5 and Appendix A.2.

6. Discussion

6.1. Ages of magmatism and metallogenesis

Geochronological data published in the region are listed in Table 1. These data are from 11 typical hydrothermal, skarn-type, and porphyry-type deposits in the Huanggang–Ganzhuermiao polymetallic metallogenic belt (Table 1). The belt records five periods of magmatism (during ca. 326–300, ca. 292–279, ca. 254–239, ca. 170 and ca. 147–129 Ma) and two periods of metallogenesis (during ca. 244–242 and ca. 150–130 Ma) (Table 1; Fig. 12). The peak of the magmatism and metallogenesis in the belt took place during 250–240 Ma and 150–130 Ma (Fig. 12).

The dates of the felsic units at Shuangjianzishan determined for this study are 254–252 Ma for the porphyritic monzogranite, 169 Ma for the rhyolitic crystal–vitric ignimbrite, and 130 Ma for the porphyritic granodiorite. Wu et al. (2013) reported a LA-ICP-MS zircon U–Pb date of 239 ± 1 Ma for quartz porphyry dykes in the area. We obtained a Re–Os isochron age of 165 ± 7 Ma on pyrite from the area, and Wu et al. (2013) report a Rb–Sr isochron age for sphalerite of 133 ± 4 Ma. Thus, the data indicate that the ages of the magmatic activities associated with two periods of metallogenesis in the Shuangjianzishan district are ca. 170 and ca. 130 Ma.

Table 2
Re–Os isotopic data for pyrite from the Shuangjianzishan Pb–Zn–Ag deposit.

Sample	Weight (g)	Re (ng/g)		Common Os (ng/g)		^{187}Os (ng/g)		$^{187}Re/^{188}Os$		$^{187}Os/^{188}Os$	
		Measured	2σ	Measured	2σ	Measured	2σ	Measured	2σ	Measured	2σ
14SJ16	0.70432	0.0854	0.0007	0.0212	0.0002	0.002341	0.000018	19.38	0.20	0.8447	0.0051
14SJ99	0.70065	0.0384	0.0001	0.0029	0.0000	0.000368	0.000002	63.13	0.66	0.9625	0.0063
14SJ106	0.70064	0.0215	0.0001	0.0227	0.0001	0.002364	0.000008	4.57	0.05	0.8017	0.0029
14SJ19	0.70060	0.0626	0.0003	0.0120	0.0000	0.001208	0.000004	25.25	0.28	0.7758	0.0034
14SJ101	0.70222	0.0815	0.0003	0.0038	0.0000	0.000492	0.000002	103.53	1.07	0.9953	0.0021

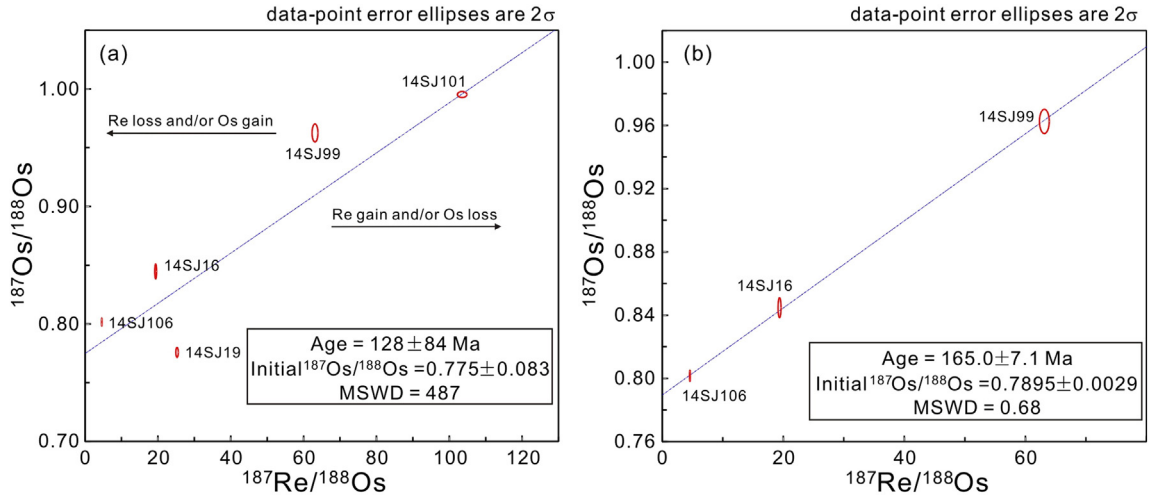

Fig. 8. Re–Os isochron plot for pyrite samples from the Shuangjianzishan Pb–Zn–Ag deposit.

6.2. Magma source and petrogenesis

The geochemical characteristics of typical adakitic rocks include high Sr contents (>300 ppm), low Y contents (<15 ppm), high Sr/Y ratios (>20), low Yb contents (<1.9 ppm), high La/Yb ratios (>20), low HFSE contents (e.g., Nb and Ta), and an absence of negative Eu anomalies (Castillo, 2006; Zhang et al., 2010c). Zhang et al. (2010c) suggest that typical adakitic rocks provide evidence for the subduction of an oceanic crust and that they should be strictly defined in a crustal-derived context.

The Sr contents for the porphyritic granodiorite in the Shuangjianzishan district are 316–417 ppm, Y contents are 4.06–4.66 ppm, Sr/Y ratios are 73.83–90.08, Yb contents are 0.35–0.4 ppm, and La_N/Yb_N ratios are 17.43–21.55. The granodiorite is also depleted in Nb and Ta, and δEu values are 0.8–1.02 (Table 3).

The ore-bearing porphyritic monzogranite in the area has a Sr content of 101–137 ppm, Y content of 9.15–12.17 ppm, Sr/Y ratios of 8.28–14.96, Yb content of 0.85–1.03 ppm, and La_N/Yb_N ratios of 10.9–19.88. The monzogranite is also depleted in Nb and Ta, with δEu values of 0.69–0.77 (Table 3). The porphyritic granodiorite is adakitic using the definition outlined above, but the geochemistry of the ore-bearing porphyritic monzogranite is not exactly typical of adakites (Fig. 13). Data for the rhyolitic crystal–vitric ignimbrite fall in arc-magmatic field on Fig. 13. The $\varepsilon_{Hf}(t)$ values for zircons from the porphyritic granodiorite are −11.34 to −1.41, their t_{DM2} ages are 1275–1901 Ma. Considering that the granodiorite is adakitic, its source was probably the lower crust and derived from subducted oceanic crust. The $\varepsilon_{Hf}(t)$ values for zircons from the rhyolitic crystal–vitric ignimbrite and the ore-bearing porphyritic monzogranite are 7.57–16.23 and 10.18–15.96, respectively, and their t_{DM2} ages are 177–733 and 257–632 Ma, respectively. This indicates that the source has the characteristics of a depleted mantle. Most Phanerozoic granitoids of Central Asia are characterized by low initial Sr isotopic ratios, positive $\varepsilon_{Nd}(T)$ values and young Sm–Nd model ages (T_{DM}) of 300–1200 Ma (Jahn et al., 2000). The isotope data indicate their 'juvenile' character and suggest their derivation from source rocks or magmas separated shortly before from the upper mantle (Jahn et al., 2000). Granitoids with negative $\varepsilon_{Nd}(T)$ values also exist, their isotope compositions may reflect contamination by the older crust in the magma generation processes (Jahn et al., 2000). The magma source and petrogenesis of the felsic magmatic rocks in the Shuangjianzishan Pb–Zn–Ag district according to the geochemical data and the $\varepsilon_{Hf}(t)$ values for zircons agree with the conclusion from the Sm–Nd data.

In summary, subducted oceanic crust is the source for the ca. 130 Ma porphyritic granodiorite, and partial melting of depleted mantle lead to the emplacement of the ca. 169 Ma rhyolitic crystal–vitric ignimbrite and the ca. 254–252 Ma ore-bearing monzogranite porphyry.

6.3. Tectonic setting

The southern part of the Great Xing'an Mountains includes accreted terranes associated with the Paleo-Asian Ocean, Mongolia–Okhotsk Ocean, and Paleo-Pacific tectonic–metallogenic domains (Bai et al., 2014; Cao et al., 2013; Chen et al., 2009, 2011, 2015; Jian et al., 2010; Ouyang et al., 2013, 2014; Tong et al., 2015; Xiao et al., 2003; Xu et al., 2015; Zeng et al., 2012, 2014a, 2014b, 2015). This makes the region geologically complex involving multiple periods of magmatic events (326–301, 287–251, 248–216, 182–160, and 146–119 Ma; Ouyang, 2013) and metallogenic events (Shao et al., 1997; Wang et al., 2012).

There are differing hypotheses on the tectonic setting of large-scale Mesozoic crustal uplift and magmatic activity in the Great Xing'an Mountains (Mao et al., 2003; Yang et al., 2003; Zhang et al., 2008a, 2008b, 2010a, 2011, 2013a, 2013b; Ying et al., 2010; Zeng et al., 2012, 2013a, b, 2014a, b, 2015; Zhu et al., 2011; Ouyang et al., 2013; Li and Santosh, 2014). In addition, the Paleozoic history of the region has been proposed by various authors who have associated the tectonic events with the eventual closure of the Paleo-Asian Ocean, which is now represented by the Solonker–Xar Moron–Changchun Suture (e.g. Cao et al., 2013; Robinson et al., 1999; Xiao et al., 2003; Wu et al., 2007, 2011; Zhang et al., 2009c). This includes the emplacement of Carboniferous intrusive rocks in the southern part of the Great Xing'an Mountains, which is related to the bi-directional subduction of the Paleo-Asian Ocean (Liu et al., 2009). The Permian intrusive rocks are interpreted as being related to the break-off and delamination of a Paleo-Asian Ocean slab, upwelling of the asthenosphere, and partial melting of the overlying lithospheric mantle and lower crust (Ouyang, 2013).

The Mesozoic metallogenesis in northeast China and adjacent areas can be subdivided into five periods (240–205, 190–165, 155–145, 140–120, and 115–100 Ma), which reflect the closure of the Paleo-Asian, Mongolia–Okhotsk and Paleo-Pacific oceans (Li et al., 2012; Ouyang et al., 2013). The period 240–205 Ma corresponds to the post-orogenic extension that followed closure of the Paleo-Asian Ocean. Subduction of the Mongolia–Okhotsk Ocean in the Argun area took place at 190–165 Ma (Bai et al., 2014; Chen et al., 2011; Dai et al.,

Table 3
Major (wt.%) and trace element (ppm) compositions of felsic magmatic rocks at the Shuangjianzishan Pb–Zn–Ag deposit.

Sample	14SJ50-1	14SJ50-2	14SJ52-1	14SJ52-2	14SJ64-1	14SJ64-2	14SJ65-1	14SJ65-2	14SJ93-1	14SJ93-2	14SJ93-3	14SJ122	14SJ123	14SJ124
	Rhyolitic crystal–vitric ignimbrite				Porphyritic granodiorite				Ore-bearing porphyritic monzogranite					
SiO_2	77.63	77.73	77.36	77.65	71.40	71.40	71.79	71.82	67.14	66.91	67.04	66.75	66.69	65.68
TiO_2	0.09	0.09	0.09	0.09	0.25	0.25	0.27	0.26	0.65	0.65	0.64	0.65	0.64	0.71
Al_2O_3	12.32	12.24	12.26	12.17	15.60	15.67	15.54	15.52	16.10	16.12	16.19	16.32	16.61	16.90
Fe_2O_3	0.81	0.75	0.99	1.02	0.18	0.17	0.21	0.28	0.66	0.61	0.72	1.17	1.03	1.87
FeO	0.22	0.26	0.26	0.22	1.17	1.17	0.96	0.91	3.14	3.23	3.09	2.85	2.61	2.18
MnO	0.34	0.34	0.25	0.26	0.03	0.03	0.03	0.03	0.15	0.15	0.15	0.16	0.14	0.13
MgO	0.32	0.31	0.33	0.26	0.68	0.68	0.62	0.62	1.15	1.19	1.19	1.09	1.26	1.09
CaO	0.25	0.25	0.30	0.30	1.81	1.82	1.80	1.80	0.43	0.43	0.44	0.43	0.46	0.44
Na_2O	0.16	0.17	0.16	0.16	5.89	5.83	5.82	5.82	3.36	3.39	3.32	3.29	3.03	2.08
K_2O	5.16	5.19	4.96	4.93	1.67	1.68	1.55	1.56	3.93	3.95	3.94	4.32	4.33	4.99
P_2O_5	0.02	0.02	0.02	0.02	0.08	0.09	0.09	0.09	0.20	0.20	0.20	0.20	0.20	0.22
LOI	2.41	2.41	2.75	2.66	1.09	1.09	1.23	1.19	2.42	2.47	2.40	2.47	2.63	3.30
Total	99.75	99.77	99.74	99.73	99.87	99.89	99.90	99.91	99.32	99.31	99.32	99.71	99.64	99.59
Q	58.09	57.98	58.78	59.22	25.9	26.23	27.55	27.59	30.62	29.97	30.71	29.46	30.92	34.42
An	1.12	1.12	1.37	1.37	8.3	8.29	8.19	8.19	0.85	0.85	0.91	0.85	1.01	0.78
Ab	1.44	1.52	1.44	1.44	51.54	51.03	50.96	50.93	30.93	31.24	30.58	30.16	27.87	19.38
Or	33.09	33.25	31.97	31.73	10.45	10.51	9.7	9.76	25.86	26.02	25.94	28.31	28.47	33.23
A/CNK	2.02	1.99	2.07	2.07	1.19	1.20	1.21	1.20	1.58	1.57	1.60	1.56	1.64	1.83
A/NK	2.10	2.07	2.17	2.17	1.36	1.37	1.38	1.38	1.64	1.63	1.66	1.62	1.72	1.91
$Mg^{\#}$	0.38	0.37	0.34	0.29	0.48	0.48	0.49	0.49	0.36	0.36	0.36	0.34	0.39	0.34
La	27.03	27.65	27.43	25.26	9.44	8.80	10.66	10.45	23.69	26.79	24.48	12.89	24.18	18.06
Ce	65.58	66.30	66.73	60.74	20.52	19.30	22.68	21.92	52.85	59.51	54.83	30.89	50.65	44.69
Pr	8.82	8.85	8.90	8.03	2.62	2.43	2.84	2.66	6.39	7.21	6.64	4.02	6.21	5.47
Nd	37.39	37.03	37.06	33.58	10.64	10.12	11.45	10.84	24.34	27.50	25.86	16.07	24.15	22.10
Sm	9.24	9.32	9.28	8.45	1.72	1.63	1.85	1.70	3.82	4.12	3.98	2.70	3.76	3.80
Eu	0.13	0.14	0.14	0.14	0.51	0.52	0.47	0.44	0.84	0.96	0.92	0.66	0.90	0.83
Gd	7.93	8.07	7.99	7.18	1.46	1.46	1.64	1.50	3.44	3.86	3.53	2.46	3.44	3.41
Tb	1.69	1.67	1.70	1.53	0.22	0.20	0.23	0.22	0.46	0.50	0.47	0.40	0.47	0.50
Dy	10.19	10.20	10.63	9.68	0.99	0.84	0.97	0.95	2.08	2.30	2.16	2.02	2.19	2.48
Ho	2.00	2.03	2.13	1.91	0.17	0.16	0.17	0.16	0.36	0.40	0.39	0.35	0.38	0.43
Er	5.29	5.24	5.77	5.06	0.43	0.38	0.43	0.40	0.92	1.05	0.96	0.84	0.95	1.08
Tm	0.98	0.98	1.09	0.98	0.07	0.06	0.06	0.06	0.15	0.16	0.16	0.14	0.14	0.17
Yb	6.23	6.28	7.19	6.37	0.39	0.36	0.40	0.35	0.86	0.99	0.96	0.85	0.88	1.03
Lu	1.08	1.08	1.21	1.09	0.12	0.12	0.13	0.13	0.32	0.35	0.34	0.31	0.31	0.35
Y	56.63	58.10	61.37	55.53	4.66	4.06	4.28	4.09	9.96	11.09	10.62	9.15	10.65	12.17
ΣREE	184	185	187	170	49	46	54	52	121	136	126	75	119	104
LREE	148	149	150	136	45	43	50	48	112	126	117	67	110	95
HREE	35.38	35.55	37.72	33.79	3.85	3.57	4.03	3.77	8.57	9.61	8.97	7.37	8.76	9.44
L/H	4.19	4.20	3.96	4.03	11.81	11.99	12.39	12.75	13.06	13.12	13.02	9.13	12.54	10.05
La_N/Yb_N	3.11	3.16	2.74	2.85	17.43	17.57	19.21	21.55	19.88	19.33	18.30	10.90	19.76	12.63
δEu	0.05	0.05	0.05	0.05	0.96	1.02	0.80	0.83	0.70	0.73	0.73	0.77	0.75	0.69
δCe	1.04	1.03	1.04	1.04	0.99	1.01	0.99	0.99	1.03	1.03	1.03	1.04	0.99	1.09
Li	34.83	33.52	29.06	27.48	50.09	38.82	45.18	53.17	35.46	39.40	35.65	32.49	31.28	28.21
Be	8.12	7.53	6.51	7.04	1.75	1.55	1.14	1.36	1.86	1.66	1.84	2.00	2.01	2.29
Sc	5.96	5.90	6.19	5.78	5.65	4.93	4.86	6.14	8.26	9.13	7.92	8.15	8.85	8.43
V	28.99	29.08	20.33	17.97	28.12	25.57	25.73	40.47	44.80	50.52	43.12	41.62	47.85	49.35
Cr	5.22	4.98	3.94	3.41	7.29	6.25	6.37	9.36	14.17	15.44	13.69	13.11	13.46	14.46
Co	1.16	1.14	1.25	1.08	3.23	2.96	4.90	4.53	8.06	9.04	8.28	7.90	8.34	8.37
Ni	11.82	1.51	10.73	1.50	3.96	3.02	2.74	2.91	8.81	10.15	9.80	8.88	9.91	9.09
Cu	1.81	0.82	0.69	0.79	4.28	3.71	3.66	3.81	33.24	37.74	35.77	10.62	32.09	22.08
Zn	1189	1199	1192	1304	26	23	47	50	2063	2284	2195	390	717	520
Ga	27.47	25.39	23.62	23.33	19.75	18.85	18.34	19.60	21.52	24.11	22.67	22.50	23.86	23.46
Rb	329	336	314	302	64	32	35	67	127	134	105	141	124	185
Sr	61	58	55	52	417	323	316	369	121	136	122	137	127	101
Zr	217	213	240	214	123	132	126	126	219	221	245	241	199	220
Nb	32.05	30.02	27.96	27.97	1.71	1.61	1.78	1.81	8.09	8.70	8.24	7.67	7.84	8.37
Mo	0.31	0.15	0.33	0.17	0.57	0.61	0.14	0.13	0.26	0.08	0.29	0.20	0.08	0.23
Ag	0.35	0.42	0.38	0.34	0.04	0.06	0.16	0.13	7.94	8.79	8.20	0.98	1.53	5.74
Cd	0.10	0.24	1.25	1.25	0.09	0.05	0.20	0.27	16.19	18.52	16.72	1.57	3.70	0.99
In	0.09	0.07	0.06	0.07	0.01	0.01	0.01	0.02	0.08	0.10	0.09	0.07	0.05	0.05
Sb	2.31	1.93	2.16	2.01	0.32	0.28	0.37	0.28	5.20	5.69	5.40	2.49	2.75	5.36
Cs	24.40	23.84	22.14	21.10	4.61	3.70	3.00	4.42	10.25	11.15	9.61	14.92	12.52	20.26
Ba	164	163	171	168	263	219	212	239	745	822	770	804	724	789
Hf	9.53	9.64	10.18	9.20	4.03	4.44	4.16	4.19	5.35	5.52	6.19	6.14	5.37	5.68
Ta	2.73	2.30	2.08	2.18	0.40	0.19	0.24	0.44	0.59	0.88	0.63	0.70	0.74	0.79
W	0.82	0.77	0.56	0.55	0.84	0.79	1.22	1.30	2.47	2.56	2.52	1.20	1.03	1.76
Tl	5.45	5.08	5.66	5.97	0.55	0.35	0.27	0.30	2.39	2.46	2.37	2.78	2.75	4.34
Pb	22.00	20.55	91.48	92.24	7.47	6.20	41.75	44.20	1641	1789	1736	335	472	1081
Bi	0.30	0.27	0.28	0.28	0.10	0.09	0.08	0.07	0.25	0.27	0.26	0.24	0.31	1.04
Th	35.14	35.71	35.83	34.09	4.69	1.86	1.93	2.76	10.79	11.55	9.15	10.58	8.91	11.74
U	6.93	6.62	7.83	7.58	0.78	0.46	0.64	0.79	2.67	2.96	2.67	2.48	2.47	2.62
Sr/Y	1.08	1.01	0.89	0.94	89.53	79.54	73.83	90.08	12.16	12.23	11.53	14.96	11.96	8.28

$\delta Eu = (Eu)_N/[(Gd)_N + (Sm)_N]^{1/2}$; $\delta Ce = (Ce)_N/[(La)_N + (Pr)_N]^{1/2}$; LREE = La + Ce + Pr + Nd + Sm + Eu; HREE = Gd + Tb + Dy + Ho + Er + Tm + Yb + Lu; ΣREE = LREE + HREE; $(La/Yb)_N = (La/0.237)/(Yb/0.170)$; L/H = LREE/HREE; LOI = loss on ignition; A/CNK = mole $[Al_2O_3/(CaO + Na_2O + K_2O)]$; A/NK = mole $[Al_2O_3/(Na_2O + K_2O)]$; $Mg^{\#}$ = mole $[Mg^{2+}/(Mg^{2+}+Fe^{2+}+Fe^{3+})]$.

2009; Han et al., 2009; Zeng et al., 2015; Zhang et al., 2009a). The period 155–145 Ma corresponds to post-orogenic extension that followed closure of the Mongolia–Okhotsk Ocean, and the period 140–120 Ma relates to an extensional environment that was the result of the closure of the Mongolia–Okhotsk Ocean and the subduction of the Paleo-Pacific Ocean Plate (Dong et al., 2014; Fu et al., 2014; Ma et al., 2015). The period 115–100 Ma corresponds to the stage of transformation from lithospheric extension associated with the upwelling of asthenospheric material to compressional tectonics following the cessation of the subduction of the Paleo-Pacific Ocean Plate (Ouyang et al., 2013; Wu et al., 2011).

The ca. 254–252 Ma porphyritic monzogranite were emplaced during the late stages of closure of the Paleo-Asian Ocean corresponding to a collisional event. During this time, the region underwent a transition from a collisional to an extensional tectonic setting. We therefore propose that the genesis of the rhyolitic crystal–vitric ignimbrite relates to the closure of the Mongolia–Okhotsk Ocean.

The ca. 170 and ca. 130 Ma mineralization in the Shuangjianzishan area are related to subduction of the Mongolia–Okhotsk Ocean and subduction of the Paleo-Pacific Ocean Plate, respectively. The porphyritic granodiorite is interpreted as being adakitic, based on its geochemistry, and related to the subduction of the Paleo-Pacific oceanic plate.

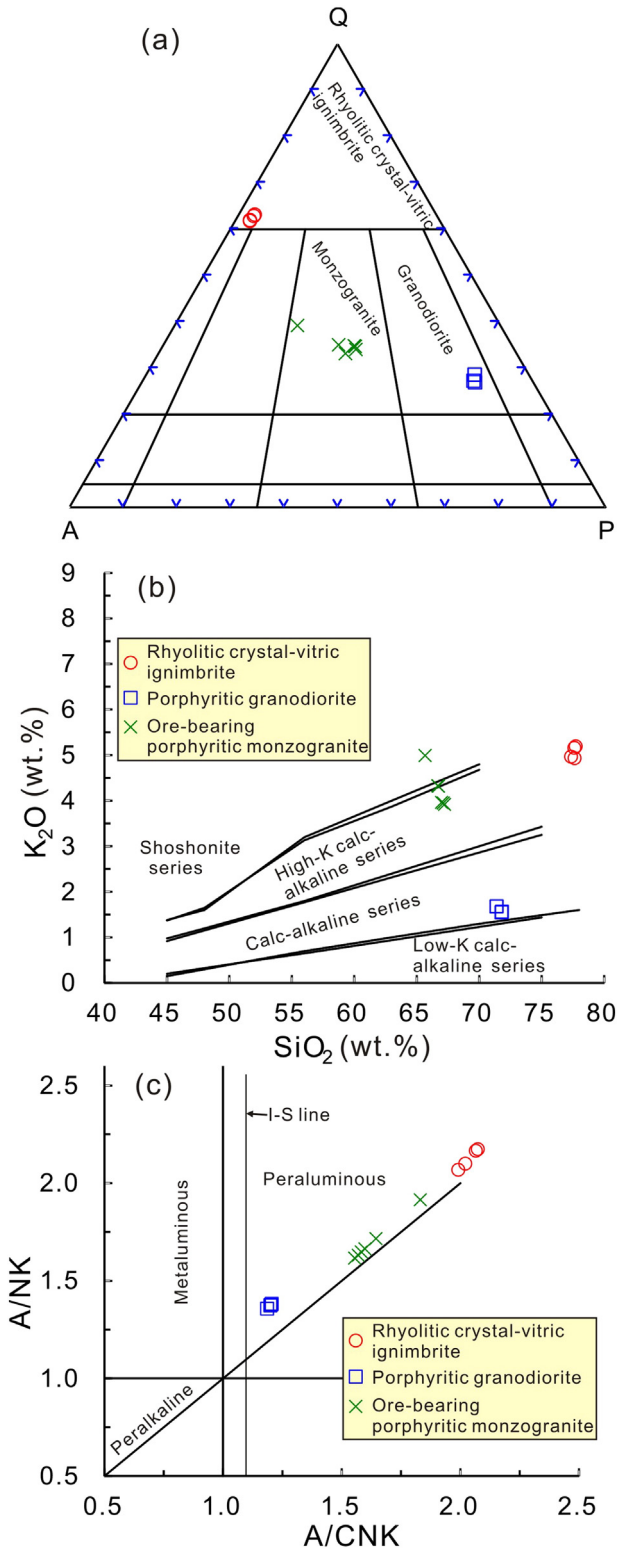

Fig. 9. Geochemical analyses of felsic magmatic rocks at the Shuangjianzishan Pb–Zn–Ag deposit represented by: (a) Q–A–P diagram (Streckeisen, 1976); (b) K_2O versus SiO_2 diagram (Rollinson, 1993); and (c) alumina saturation diagram (Maniar and Piccoli, 1989).

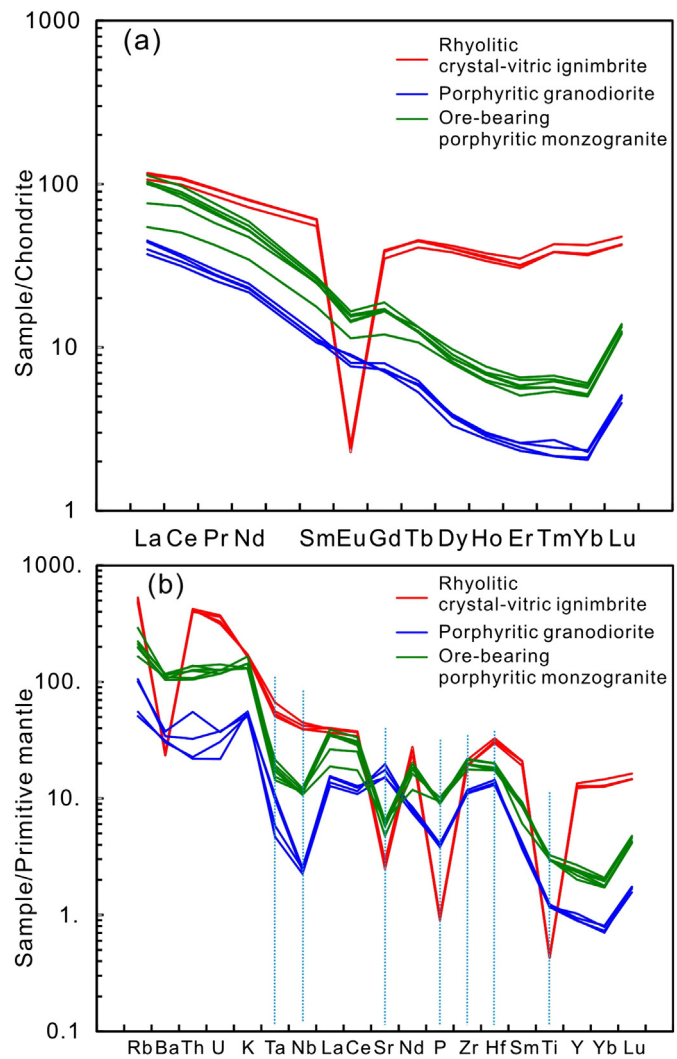

Fig. 10. (a) Chondrite-normalized rare earth element (REE) patterns for magmatic rocks in the Shuangjianzishan Pb–Zn–Ag deposit. Normalizing values are from Sun and McDonough (1989). (b) Primitive-mantle-normalized trace element patterns for magmatic rocks in the Shuangjianzishan Pb–Zn–Ag deposit. Normalizing values are from Sun and McDonough (1989).

Table 4
Sr and Sr/Y values for felsic magmatic rocks at Shuangjianzishan.

Rock types	Sr (ppm)	Sr/Y
Porphyritic granodiorite	316–417	73.83–90.08
Ore-bearing porphyritic monzogranite	101–137	8.28–14.96
Rhyolitic crystal–vitric ignimbrite	52–61	0.89–1.08

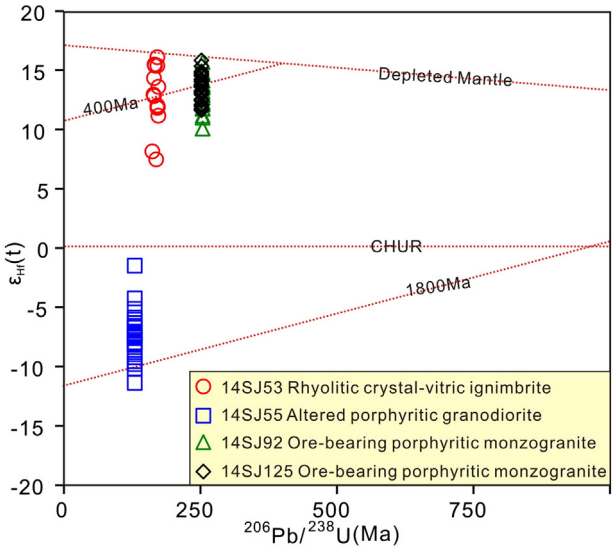

Fig. 11. Zircon $\varepsilon_{Hf}(t)$ versus $^{206}Pb/^{238}U$ diagram for magmatic rocks at the Shuangjianzishan Pb–Zn–Ag deposit.

7. Conclusions

The main results and conclusions of this study are summarized as follows:

This contribution shows that the felsic magmatic rocks in the Shuangjianzishan Pb–Zn–Ag district are generally characterized by LREE enrichment, HREE depletion, Nb, Ta, P, and Ti depletion, and Zr and Hf enrichment.

The ages of the monzogranite porphyry, rhyolitic crystal–vitric ignimbrite, and granodiorite porphyry are 254–252, 169, and 130 Ma, respectively. The pyrite Re–Os isochron age is 165 ± 7 Ma. The ages of the magmatic activities associated with the metallogenetic in the Shuangjianzishan district are ca. 170 and ca. 130 Ma.

The origin of the 254–252 and 169 Ma magma in the Shuangjianzishan district included partial melting of depleted mantle. The dehydration partial melting of subducted oceanic crust resulted in the formation of granodiorite porphyry (130 Ma).

Monzogranite porphyries in the ore district with ages of 254–252 Ma formed during the late stages of closure of the Paleo-Asian Ocean (during the transformation from a collisional to extensional tectonic setting). The ca. 170 and ca. 130 Ma mineralizations in the Shuangjianzishan district is related to subduction of the Mongolia–Okhotsk Ocean and subduction of the Paleo-Pacific Ocean Plate, respectively.

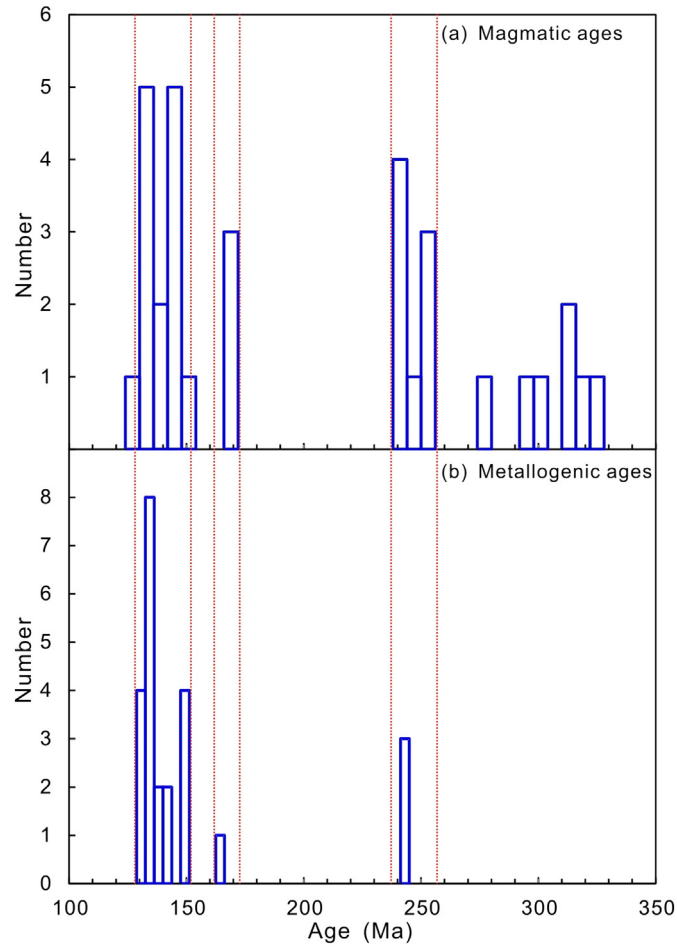

Fig. 12. Ages of magmatic rocks and typical deposits in the Huanggang–Ganzhuermiao metallogenic belt.

Supplementary data to this article can be found online at http://dx.doi.org/10.1016/j.oregeorev.2015.12.019.

Acknowledgments

This study was financially supported by the Major State Basic Research Program of China (no. 2013CB429805), National Natural Science Foundation of China (no. 41502084), and China Postdoctoral Science Foundation (2015M570128). We also acknowledge the Australian Research Council (ARC) Linkage Project LP110100667 and the ARC Centre of Excellence for Core to Crust Fluid Systems (CCFS) (LP110100667). We sincerely appreciate the great support and assistance provided by the Chifeng Tiantong Geological Exploration Co. Ltd., Inner Mongolia, China. We are grateful to Dr. Qingdong Zeng and Sihong Jiang for their constructive comments on this manuscript. We thank the editor-in-chief Franco Pirajno for his revision on this manuscript.

Table 5
Hf isotope analyses for zircons from felsic magmatic rocks at Shuangjianzishan.

Sample no.	Rock types	$\varepsilon_{Hf}(t)$	Single-stage Hf model (t_{DM1}) age (Ma)	Two-stage Hf model (t_{DM2}) age (Ma)
14SJ53	Rhyolitic crystal–vitric ignimbrite (n = 15)	7.57–16.23	175–524	177–733
14SJ55	Porphyritic granodiorite (n = 25)	−11.34 to −1.41	879–1242	1275–1901
14SJ92	Ore-bearing porphyritic monzogranite (n = 27)	10.18–15.81	263–489	269–632
14SJ125	Ore-bearing porphyritic monzogranite (n = 25)	11.75–15.96	255–425	257–530

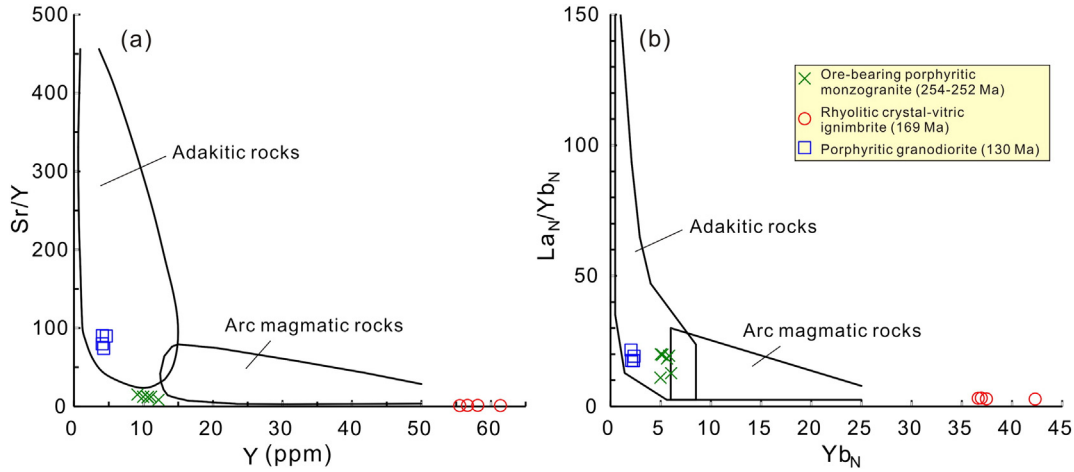

Fig. 13. Diagrams for magmatic rocks at the Shuangjianzishan Pb–Zn–Ag deposit: (a) Sr/Y versus Y (Defant and Drummond, 1990); and (b) La_N/Yb_N versus Yb_N (Martin, 1986).

References

Akiyama, S., Sun, S.H., 2001. A special issue devoted to the geology and mineralization of the southern Da Hinggan Mountains area, Inner Mongolia, China. Resour. Geol. 51, 273–274.

Andersen, T., 2002. Correction of common lead in U–Pb analyses that do not report ^{204}Pb. Chem. Geol. 192, 59–79.

Bai, L.A., Sun, J.G., Gu, A.L., Zhao, K.Q., Sun, Q.L., 2014. A review of the genesis, geochronology, and geological significance of hydrothermal copper and associated metals deposits in the Great Xing'an Range, NE China. Ore Geol. Rev. 61, 192–203.

Cao, H.H., Xu, W.L., Pei, F.P., Wang, Z.W., Wang, F., Wang, Z.J., 2013. Zircon U–Pb geochronology and petrogenesis of the Late Paleozoic–Early Mesozoic intrusive rocks in the eastern segment of the northern margin of the North China Block. Lithos 170, 191–207.

Castillo, P.R., 2006. An overview of adakite petrogenesis. Chin. Sci. Bull. 51 (3), 257–268.

Chang, Y., Lai, Y., 2010. Study on characteristics of ore-forming fluid and chronology in the Yindu Ag–Pb–Zn polymetallic ore deposit, Inner Mongolia. Acta Sci. Nat. Univ. Pekin. 46, 581–593 (in Chinese with English abstract).

Chen, B., Jahn, B.M., Tian, W., 2009. Evolution of the Solonker suture zone: constraints from zircon U–Pb ages, Hf isotopic ratios and whole-rock Nd–Sr isotope compositions of subduction- and collision-related magmas and forearc sediments. J. Asian Earth Sci. 34 (3), 245–257.

Chen, J.F., Han, B.F., Ji, J.Q., Zhang, L., Xu, Z., He, G.Q., Wang, T., 2010. Zircon U–Pb ages and tectonic implications of Paleozoic plutons in northern West Junggar, North Xinjiang, China. Lithos 115 (1), 137–152.

Chen, Z.G., Zhang, L.C., Wan, B., Wu, H.Y., Cleven, N., 2011. Geochronology and geochemistry of the Wunugetushan porphyry Cu–Mo deposit in NE China, and their geological significance. Ore Geol. Rev. 43 (1), 92–105.

Chen, C., Zhang, Z.C., Li, K., Chen, Y., Tang, W.H., Li, J.F., 2015. Geochronology, geochemistry, and its geological significance of the Damaoqi Permian volcanic sequences on the northern margin of the North China Block. J. Asian Earth Sci. 97, 307–319.

Cheng, Y.H., Teng, X.J., Li, Y.F., Li, M., Zhang, T.F., 2014. Early Permian East-Ujimqin mafic–ultramafic and granitic rocks from the Xing'an–Mongolian Orogenic Belt, North China: origin, chronology, and tectonic implications. J. Asian Earth Sci. 96, 361–373.

Dai, J.Z., Mao, J.W., Zhao, C.S., Xie, G.Q., Yang, F.Q., Wang, Y.T., 2009. New U–Pb and Re–Os age data and the geodynamic setting of the Xiaojiayingzi Mo (Fe) deposit, western Liaoning province, northeastern China. Ore Geol. Rev. 35 (2), 235–244.

Defant, M.J., Drummond, M.S., 1990. Derivation of some modern arc magmas by melting of young subducted lithosphere. Nature 347, 662–665.

Dong, Y., Ge, W.C., Yang, H., Zhao, G.H., Wang, Q.H., Zhang, Y.L., Su, L., 2014. Geochronology and geochemistry of Early Cretaceous volcanic rocks from the Baiyingaolao Formation in the central Great Xing'an Range, NE China, and its tectonic implications. Lithos 205, 168–184.

Du, A.D., He, H.L., Yin, N.W., 1995. A study of the rhenium–osmium geochronometry of molybdenites. Acta Geol. Sin.(English Edition) 8, 171–181.

Du, A.D., Wang, S.X., Sun, D., Zhao, D., Liu, D., 2001. Precise Re–Os dating of molybdenite using Carius tube, NTIMS and ICPMS. In: Piestrzynski (Ed.), Mineral Deposits at the 21st Century, pp. 405–407.

Du, A.D., Wu, S.Q., Sun, D.Z., Wang, S.X., Qu, W.J., Markey, R., Stein, H., Morgan, J.W., Malinovskiy, D., 2004. Preparation and certification of Re–Os dating reference materials: molybdenite HLP and JDC. Geostand. Geoanal. Res. 28, 41–52.

Elhlou, S., Belousova, E., Griffin, W.L., Pearson, N.J., O'Reilly, S.Y., 2006. Trace element and isotopic composition of GJ-red zircon standard by laser ablation. Geochim. Cosmochim. Acta 70, A158.

Fu, L.B., Wei, J.H., Chen, H.Y., Bagas, L., Tan, J., Li, H., Zhang, D.H., Tian, N., 2014. The relationship between gold mineralization, exhumation of metamorphic core complex and magma cooling: formation of the Anjiayingzi Au deposit, northern North China Craton. Ore Geol. Rev. http://dx.doi.org/10.1016/j.oregeorev.2014.09.025.

Han, C.M., Xiao, W.J., Zhao, G.C., Sun, M., Qu, W.J., Du, A.D., 2009. A Re–Os study of molybdenites from the Lanjiagou Mo deposit of North China Craton and its geological significance. Gondwana Res. 16 (2), 264–271.

Hong, D.W., Wang, S.G., Xie, X.L., Zhang, J.S., Wang, T., 2003. Metallogenic province derived from mantle sources: Nd, Sr, S and Pb isotope evidence from the Central Asian orogenic belt. Gondwana Res. 6, 711–728.

Hou, K.J., Li, Y.H., Zou, T.R., Qu, X.M., Shi, Y.R., Xie, G.Q., 2007. Laser ablation-MC-ICP-MS technique for Hf isotope microanalysis of zircon and its geological applications. Acta Petrol. Sin. 23, 2595–2604 (in Chinese with English abstract).

Hu, C.S., Li, W.B., Xu, C., Zhong, R.C., Zhu, F., 2015. Geochemistry and zircon U–Pb–Hf isotopes of the granitoids of Baolidao and Halatu plutons in Sonidzuoqi area, Inner Mongolia: implications for petrogenesis and geodynamic setting. J. Asian Earth Sci. 97, 294–306.

Ishiyama, D., Sato, R., Mizuta, T., Ishikawa, Y., Wang, J.B., 2001. Characteristic features of tin–iron–copper mineralization in the Anle–Huanggangliang Mining Area, Inner Mongolia, China. Resour. Geol. 51, 377–392.

Jahn, B.M., Wu, F.Y., Chen, B., 2000. Granitoids of the Central Asian Orogenic Belt and continental growth in the Phanerozoic. Trans. Roy. Soc. Edinb. Earth Sci. 91, 181–193.

Jian, P., Liu, D.Y., Kröner, A., Windley, B.F., Shi, Y.R., Zhang, F.Q., Shi, G.H., Miao, L.C., Zhang, W., Zhang, Q., Zhang, L.Q., Ren, J.S., 2008. Time scale of an early to mid-Paleozoic orogenic cycle of the long-lived Central Asian Orogenic Belt, Inner Mongolia of China: implications for continental growth. Lithos 101 (3), 233–259.

Jian, P., Liu, D.Y., Kröner, A., Windley, B.F., Shi, Y.R., Zhang, W., Zhang, F.Q., Miao, L.C., Zhang, L.Q., Tomurhuu, D., 2010. Evolution of a Permian intraoceanic arc–trench system in the Solonker suture zone, Central Asian Orogenic Belt, China and Mongolia. Lithos 118 (1), 169–190.

Jiang, S.H., Nie, F.J., Bai, D.M., Liu, Y.F., Liu, Y., 2011. Geochronology evidence for Indosinian mineralization in Baiyinnuoer Pb–Zn deposit of Inner Mongolia. Mineral Deposits 30, 787–798 (in Chinese with English abstract).

Jiang, S.H., Liang, Q.L., Liu, Y.F., Liu, Y., 2012. Zircon U–Pb ages of magmatic rocks occurring in around the Dajing Cu–Ag–Sn polymetallic deposit of Inner Mongolia constrains to the ore-forming age. Acta Petrol. Sin. 28, 495–513 (in Chinese with English abstract).

Li, S.R., Santosh, M., 2014. Metallogeny and craton destruction: records from the North China Craton. Ore Geol. Rev. 56, 376–414.

Li, Y.L., Zhou, H.W., Brouwer, F.M., Wijbrans, J.R., Zhong, Z.Q., Liu, H.F., 2011. Tectonic significance of the Xilin Gol Complex, Inner Mongolia, China: petrological, geochemical and U–Pb zircon age constraints. J. Asian Earth Sci. 42 (5), 1018–1029.

Li, S.Q., Chen, F., Siebel, W., Wu, J.D., Zhu, X.Y., Shan, X.L., Sun, X.M., 2012. Late Mesozoic tectonic evolution of the Songliao basin, NE China: evidence from detrital zircon ages and Sr–Nd isotopes. Gondwana Res. 22 (3), 943–955.

Li, S., Wilde, S.A., Wang, T., 2013. Early Permian post-collisional high-K granitoids from Liuyuan area in southern Beishan orogen, NW China: petrogenesis and tectonic implications. Lithos 179, 99–119.

Li, Y.L., Zhou, H.W., Brouwer, F.M., Xiao, W.J., Wijbrans, J.R., Zhong, Z.Q., 2014. Early Paleozoic to Middle Triassic bivergent accretion in the Central Asian Orogenic Belt: insights from zircon U–Pb dating of ductile shear zones in central Inner Mongolia, China. Lithos 205, 84–111.

Li, W.B., Hu, C.S., Zhong, R.C., Zhu, F., 2015. U–Pb, ^{39}Ar/^{40}Ar geochronology of the metamorphosed volcanic rocks of the Bainaimiao Group in central Inner Mongolia and its implications for ore genesis and geodynamic setting. J. Asian Earth Sci. 97, 251–259.

Liu, C.H., Nie, F.J., 2015. Permian magmatic sequences of the Bilihe gold deposit in central Inner Mongolia, China: petrogenesis and tectonic significance. Lithos 231, 35–52.

Liu, J.F., Chi, X.G., Zhang, X.Z., Ma, Z.H., Zhao, Z., Wang, T.F., Hu, Z.C., Zhao, X.Y., 2009. Geochemical characteristic of carboniferous quartz–diorite in the southern Xiwuqi area, Inner Mongolia and its tectonic significance. Acta Geol. Sin. 83, 365–376 (in Chinese with English abstract).

Liu, Y.F., Jiang, S.H., Zhang, Y., 2010. The SHRIMP zircon U–Pb dating and geological features of Bairendaba diorite in the Xilinhaote area, Inner Mongolia, China. Geol. Bull. China 29, 688–696 (in Chinese with English abstract).

Liu, J.F., Li, J.Y., Chi, X.G., Qu, J.F., Hu, Z.C., Fang, S., Zhang, Z., 2013. A late-Carboniferous to early early-Permian subduction–accretion complex in Daqing pasture, southeastern Inner Mongolia: evidence of northward subduction beneath the Siberian paleoplate southern margin. Lithos 177, 285–296.

Ludwig, K.R., 2003. User's Manual for Isoplot 3.00. A Geochronological Toolkit for Microsoft Excel. Berkeley Geochronology Center Special, Publication, Berkeley, pp. 1–70.
Ma, X.H., Cao, R., Zhou, Z.H., Zhu, W.P., 2015. Early Cretaceous high-Mg diorites in the Yanji area, northeastern China: petrogenesis and tectonic implications. J. Asian Earth Sci. 97, 393–405.
Maniar, P.D., Piccoli, P.M., 1989. Tectonic discrimination of granitoids. Geol. Soc. Am. Bull. 101, 635–643.
Mao, J.W., Wang, Y.T., Zhang, Z.H., Yu, J.J., Niu, B.G., 2003. Geodynamic settings of Mesozoic large-scale mineralization in the North China and adjacent areas: implication from the highly precise and accurate ages of metal deposits. Sci. China (Ser. D) 46, 838–851.
Markey, R., Stein, H., Morgan, J., 1998. Highly precise Re–Os dating for molybdenite using alkaline fusion and NTIMS. Talanta 45, 935–946.
Martin, H., 1986. Effect of steeper Archean geothermal gradient on geochemistry of subduction-zone magmas. Geology 14, 753–756.
Nie, F.J., Cao, Y., Ding, C.W., Liu, Y.F., 2014. Preliminary discussions on the rejuvenated metallogenesis of the Da Hinggan-Mongolia Paleozoic orogenic belt as deduced from the studies on Sn, W and Mo-polymetallic deposits occurring within the Xilinhot and Ergun Massifs. Acta Petrol. Sin. 30 (7), 2063–2080 (in Chinese with English abstract).
Nie, F.J., Li, Q.F., Liu, C.H., Ding, C.W., 2015. Geology and origin of Ag–Pb–Zn deposits occurring in the Ulaan-Jiawula metallogenic province, northeast Asia. J. Asian Earth Sci. 97, 424–441.
Niu, S.Y., Guo, L.J., Liu, J.M., Shao, J.A., Wang, B.D., Hu, H.B., Sun, A.Q., Wang, S., 2006. Tectonic ore-controlling in the middle-southern segment of Da Hinggan Ling, Northeast China. Chin. J. Geochem. 25, 62–70.
Ouyang, H.G., 2013. Metallogenesis of Bairendaba–Weilasituo Silver–Polymetallic Deposit and its Geodynamic Setting, in the Southern Segment of Great Xing'an Range, NE China Ph. D. Dissertation China University of Geosciences, Beijing (in Chinese with English abstract).
Ouyang, H.G., Mao, J.W., Santosh, M., Zhou, J., Zhou, Z.H., Wu, Y., Hou, L., 2013. Geodynamic setting of Mesozoic magmatism in NE China and surrounding regions: perspectives from spatio-temporal distribution patterns of ore deposits. J. Asian Earth Sci. 78, 222–236.
Ouyang, H.G., Mao, J.W., Santosh, M., Wu, Y., Hou, L., Wang, X.F., 2014. The Early Cretaceous Weilasituo Zn–Cu–Ag vein deposit in the southern Great Xing'an Range, northeast China: fluid inclusions, H, O, S, Pb isotope geochemistry and genetic implications. Ore Geol. Rev. 56, 503–515.
Pan, X.F., Guo, L.J., Wang, S., Xue, H.M., Hou, Z.Q., Tong, Y., Li, Z.M., 2009. Laser microprobe Ar–Ar dating of biotite from the Weilasituo Cu–Zn polymetallic deposit in Inner Mongolia. Acta Petrol. Mineral. 28, 475–479 (in Chinese with English abstract).
Robinson, P.T., Zhou, M.F., Hu, X.F., Reynolds, P., Bai, W.J., Yang, J.S., 1999. Geochemical constraints on the origin of the Hegenshan Ophiolite, Inner Mongolia, China. J. Asian Earth Sci. 17, 423–442.
Rollinson, H.R., 1993. Discriminating between tectonic environments using geochemical data. Using Geochemical Data: Evaluation, Presentation, Interpretation. Longman Scientific & Technical, Essex, UK, pp. 171–214.
Shao, J.A., 2007. The Uplift and Geodynamic Setting of the Greate Hinggan Range. Geological Publishing House, Beijing (in Chinese).
Shao, J.A., Mu, B.L., He, G.Q., Zhang, L.Q., 1997. Geological effects in tectonic superposition of Paleo-Pacific domain and Paleo-Asian domain in northern part of North China. Sci. China Ser. D Earth Sci. 40, 634–640.
Shao, J.A., Zhang, L.Q., Mu, B.L., 1998. Tectono-thermal evolution of middle-south section of the Da Hinggan Mountains. Sci. China Ser. D Earth Sci. 41, 570–579.
Sheng, J.F., Fu, X.Z., 1999. The Geological Characteristics and Metallogenic Environment of Copper Polymetallic Deposits From the Middle Part of the Greate Hinggan Range. Seismological Press House, Beijing (in Chinese).
Shirey, S.B., Walker, R.J., 1995. Carius tube digestion for low-bank rhenium–osmium analysis. Anal. Chem. 67, 2136–2141.
Stein, H.J., Sundblad, K., Markey, R.J., Motuza, G., 1998. Re–Os ages for Archean molybdenite and pyrite, Kuittila-Kivisuo, Finland, and Proterozoic molybdenite, Kabeliai, Lithuania: testing the chronometer in a metamorphic and metasomatic setting. Mineral. Deposita 33, 329–345.
Streckeisen, A., 1976. To each plutonic rock its proper name. Earth Sci. Rev. 12, 1–33.
Sun, S.H., Akiyama, S., 2001. Geo-tectonic position of tin polymetallic mineralization zone in the southern Da Hinggan Mountains area, Inner Mongolia, China: an introduction to this special issue. Resour. Geol. 51, 275–282.
Sun, S.S., McDonough, W.F., 1989. Chemical and isotopic systematics of oceanic basalts: implications for mantle composition and processes. Geol. Soc. 42, 313–345.
Sun, K.W., Yang, S.X., Liu, Y.L., Zhang, S.J., Zhang, L.B., Li, Z.Y., 2010. The prospecting report of the Shuangjianzishan Ag–Pb deposit, Balinzuoqi, Inner Mongolia (unpublished technical report). Tiantong geological exploration co., LTD, Chifeng City, Inner Mongolia, 1–96 (in Chinese).
Tong, Y., Jahn, B.M., Wang, T., Hong, D.W., Smith, E.I., Sun, M., Gao, J.F., Yang, Q.D., Huang, W., 2015. Permian alkaline granites in the Erenhot–Hegenshan belt, northern Inner Mongolia, China: model of generation, time of emplacement and regional tectonic significance. J. Asian Earth Sci. 97, 320–336.
Wang, G.Z., 1997. Geological characteristics and genesis of the Anle tin–copper deposit, Inner Mongolia. Mineral Deposits 16, 260–271 (in Chinese with English abstract).
Wang, J.B., Wang, Y.W., Wang, L.J., Uemoto, T., 2001a. Tin–polymetallic mineralization in the southern part of the Da Hinggan Mountains, China. Resour. Geol. 51, 283–291.
Wang, L.J., Shimazaki, H., Shiga, Y., 2001b. Skarns and genesis of the Huanggang Fe–Sn deposit, Inner Mongolia, China. Resour. Geol. 51, 359–376.
Wang, B.D., Niu, S.Y., Sun, A.Q., Hu, H.B., Liu, Y.M., Guo, L.J., Wang, S., 2008. Helium–argon isotopic tracing for the Pb–Zn–Ag polymetallic ore deposits in the central-south segment of the Da Hinggan Ling Range. Chin. J. Geochem. 27, 235–241.
Wang, M., Fan, J.Z., Wang, Z.W., Ma, Y.Y., 2009. Comprehensive prospecting model for lead–zinc deposit of Huanggang–Ganzhuermiao Metallogenic Belt, Inner Mongolia. Earth Sci. Front. 16, 318–324.
Wang, T., Guo, L., Zheng, Y.D., Donskaya, T., Gladkochub, D., Zeng, L.S., Li, J.B., Wang, Y.B., Mazukabzov, A., 2012. Timing and processes of late Mesozoic mid-lower-crustal extension in continental NE Asia and implications for the tectonic setting of the destruction of the North China Craton: mainly constrained by zircon U–Pb ages from metamorphic core complexes. Lithos 154, 315–345.
Wang, Y., Zhou, L.Y., Zhao, L.J., 2013. Cratonic reactivation and orogeny: an example from the northern margin of the North China Craton. Gondwana Res. 24 (3), 1203–1222.
Wang, T., Guo, L., Zhang, L., Yang, Q.D., Zhang, J.J., Tong, Y., Ye, K., 2015a. Timing and evolution of Jurassic–Cretaceous granitoid magmatisms in the Mongol–Okhotsk belt and adjacent areas, NE Asia: implications for transition from contractional crustal thickening to extensional thinning and geodynamic settings. J. Asian Earth Sci. 97, 365–392.
Wang, Z.Z., Han, B.F., Feng, L.X., Liu, B., 2015b. Geochronology, geochemistry and origins of the Paleozoic–Triassic plutons in the Langshan area, western Inner Mongolia, China. J. Asian Earth Sci. 97, 337–351.
Windley, B.F., Alexeiev, D., Xiao, W.J., Kröner, A., Badarch, G., 2007. Tectonic models for accretion of the Central Asian Orogenic belt. J. Geol. Soc. Lond. 164, 31–47.
Wu, F.Y., Yang, Y.H., Xie, L.W., Yang, J.H., Xu, P., 2006. Hf isotopic compositions of the standard zircons and baddeleyites used in U–Pb geochronology. Chem. Geol. 234, 105–126.
Wu, F.Y., Zhao, G.C., Sun, D.Y., Wilde, S.A., Yang, J.H., 2007. The Hulan Group: its role in the evolution of the Central Asian Orogenic Belt of NE China. J. Asian Earth Sci. 30, 542–556.
Wu, F.Y., Sun, D.Y., Ge, W.C., Zhang, Y.B., Grant, M.L., Wilde, S.A., Jahn, B.M., 2011. Geochronology of the Phanerozoic granitoids in northeastern China. J. Asian Earth Sci. 41, 1–30.
Wu, G.B., Liu, J.M., Zeng, Q.D., Sun, H.S., Liu, M.T., 2013. The metallogenic age of Shuangjianzishan Ag–Pb–Zn deposit of Greate Hinggan Range, Inner Mongolia. Acta Mineral. Sin. 33 (Supplement No.2), 619 (in Chinese).
Wu, G.B., Liu, J.M., Zeng, Q.D., Liu, M.T., Sun, H.S., Yin, Z.W., Yin, X., 2014. Occurrences of silver in the Shuangjianzishan Pb–Zn–Ag deposit and its implications for mineral processing. Earth Sci. Front. 21 (5), 105–115.
Xiao, W.J., Santosh, M., 2014. The western Central Asian Orogenic Belt: a window to accretionary orogenesis and continental growth. Gondwana Res. 25 (4), 1429–1444.
Xiao, W.J., Windley, B.F., Hao, J., Zhai, M.G., 2003. Accretion leading to collision and the Permian Solonker suture, Inner Mongolia, China: termination of the central Asian orogenic belt. Tectonics 22, 1069.
Xiao, W.J., Han, C.M., Yuan, C., Sun, M., Lin, S.F., Chen, H.L., Li, Z.L., Li, J.L., Sun, S., 2008. Middle Cambrian to Permian subduction-related accretionary orogenesis of Northern Xinjiang, NW China: implications for the tectonic evolution of central Asia. J. Asian Earth Sci. 32 (2), 102–117.
Xiao, W.J., Windley, B.F., Yong, Y., Yan, Z., Yuan, C., Liu, C.Z., Li, J.L., 2009. Early Paleozoic to Devonian multiple-accretionary model for the Qilian Shan, NW China. J. Asian Earth Sci. 35 (3), 323–333.
Xu, B., Charvet, J., Chen, Y., Zhao, P., Shi, G.Z., 2013a. Middle Paleozoic convergent orogenic belts in western Inner Mongolia (China): framework, kinematics, geochronology and implications for tectonic evolution of the Central Asian Orogenic Belt. Gondwana Res. 23 (4), 1342–1364.
Xu, W.L., Wang, F., Pei, F.P., Meng, E., Tang, J., Xu, M.J., Wang, W., 2013b. Mesozoic tectonic regimes and regional ore-forming background in NE China: constraints from spatial and temporal variations of Mesozoic volcanic rock associations. Acta Petrol. Sin. 29 (2), 339–353 (in Chinese with English abstract).
Xu, B., Zhao, P., Bao, Q.Z., Zhou, Y.H., Wang, Y.Y., Luo, Z.W., 2014. Preliminary study on the pre-Mesozoic tectonic unit division of the Xing-Meng Orogenic belt (XMOB). Acta Petrol. Sin. 30 (7), 1841–1857 (in Chinese with English abstract).
Xu, B., Zhao, P., Wang, Y.Y., Liao, W., Luo, Z.W., Bao, Q.Z., Zhou, Y.H., 2015. The pre-Devonian tectonic framework of Xing'an–Mongolia orogenic belt (XMOB) in north China. J. Asian Earth Sci. 97, 183–196.
Xue, H.M., Guo, L.J., Hou, Z.Q., Tong, Y., Pan, X.F., Zhou, X.W., 2010. SHRIMP zircon U–Pb ages of the middle Neopaleozoic unmetamorphosed magmatic rocks in the southwestern slope of the Da Hinggan Mountains, Inner Mongolia. Acta Petrol. Mineral. 29, 811–823 (in Chinese with English abstract).
Yang, J.H., Wu, F.Y., Wilde, S.A., 2003. A review of the geodynamic setting of large-scale Late Mesozoic gold mineralization in the North China Craton: an association with lithospheric thinning. Ore Geol. Rev. 23, 125–152.
Yi, J., Wei, J.H., Yao, C.L., Zhao, S.Q., Yu, C.L., Li, Q.Y., 2012. Discovery and geological significance of the Triassic intrusive rocks in the Baiyinnuoer lead–zinc deposit, Inner Mongolia: evidence from zircon U–Pb age. Geol. Sci. Technol. Inf. 31, 10–16 (in Chinese with English abstract).
Ying, J.F., Zhou, X.H., Zhang, L.C., Wang, F., 2010. Geochronological framework of Mesozoic volcanic rocks in the Great Xing'an Range, NE China, and their geodynamic implications. J. Asian Earth Sci. 39, 786–793.
Zeng, Q.D., Liu, J.M., Zhang, Z.L., Jia, C.S., Yu, C.M., Ye, J., Liu, H.T., 2009. Geology and lead-isotope study of the Baiyinnuoer Zn–Pb–Ag deposit, south segment of the Da Hinggan Mountains, northeastern China. Resour. Geol. 59, 170–180.
Zeng, Q.D., Liu, J.M., Qin, F., Zhang, Z.L., 2010a. Geochronology of the Xiaodonggou porphyry Mo deposit in northern margin of North China Craton. Resour. Geol. 60 (2), 192–202.
Zeng, Q.D., Liu, J.M., Zhang, Z.L., 2010b. Re–Os geochronology of porphyry molybdenum deposit in south segment of Da Hinggan Mountains, Northeast China. J. Earth Sci. 21, 392–401.
Zeng, Q.D., Liu, J.M., Yu, C.M., Ye, J., Liu, H.T., 2011a. Metal deposits in the Da Hinggan Mountains, NE China: styles, characteristics, and exploration potential. Int. Geol. Rev. 53 (7), 846–878.

Zeng, Q.D., Liu, J.M., Zhang, Z.L., Chen, W.J., Zhang, W.Q., 2011b. Geology and geochronology of the Xilamulun molybdenum metallogenic belt in eastern Inner Mongolia, China. Int. J. Earth Sci. 100 (8), 1791–1809.
Zeng, Q.D., Liu, J.M., Chu, S.X., Wang, Y.B., Sun, Y., Duan, X.X., Zhou, L.L., 2012. Mesozoic molybdenum deposits in the East Xingmeng orogenic belt, northeast China: characteristics and tectonic setting. Int. Geol. Rev. 54, 1843–1869.
Zeng, Q.D., Liu, J.M., Qin, K.Z., Fan, H.R., Chu, S.X., Wang, Y.B., Zhou, L.L., 2013a. Types, characteristics, and time–space distribution of molybdenum deposits in China. Int. Geol. Rev. 55 (11), 1311–1358.
Zeng, Q.D., Sun, Y., Duan, X.X., Liu, J.M., 2013b. U–Pb and Re–Os geochronology of the Haolibao porphyry Mo–Cu deposit, NE China: implications for a Late Permian tectonic setting. Geol. Mag. 150 (6), 975–985.
Zeng, Q.D., Liu, J.M., Chu, S.X., Wang, Y.B., Sun, Y., Duan, X.X., Zhou, L.L., Qu, W.J., 2014a. Re–Os and U–Pb geochronology of the Duobaoshan porphyry Cu–Mo–(Au) deposit, northeast China, and its geological significance. J. Asian Earth Sci. 79, 895–909.
Zeng, Q.D., Wang, Z.C., He, H.Y., Wang, Y.B., Zhang, S., Liu, J.M., 2014b. Multiple isotope composition (S, Pb, H, O, He, and Ar) and genetic implications for gold deposits in the Jiapigou gold belt, Northeast China. Mineral. Deposita 49 (1), 145–164.
Zeng, Q.D., Qin, K.Z., Liu, J.M., Li, G.M., Zhai, M.G., Chu, S.X., Guo, Y.P., 2015. Porphyry molybdenum deposits in the Tianshan–Xingmeng orogenic belt, northern China. Int. J. Earth Sci. 991–1023.
Zhai, D.G., Liu, J.J., Yang, Y.Q., Wang, J.P., Ding, L., Liu, X.W., Zhang, M., Yao, M.J., Su, L., Zhang, H.Y., 2012. Petrogenetic and metallogenic ages and tectonic setting of the Huangganglang Fe–Sn deposit, Inner Mongolia. Acta Petrol. Mineral. 31, 513–523 (in Chinese with English abstract).
Zhai, D.G., Liu, J.J., Wang, J.P., Yang, Y.Q., Zhang, H.Y., Wang, X.L., Zhang, Q.B., Wang, G.W., Liu, Z.J., 2014a. Zircon U–Pb and molybdenite Re–Os geochronology, and whole-rock geochemistry of the Hashitu molybdenum deposit and host granitoids, Inner Mongolia, NE China. J. Asian Earth Sci. 79, 144–160.
Zhai, D.G., Liu, J.J., Zhang, H.Y., Yao, M.J., Wang, J.P., Yang, Y.Q., 2014b. S–Pb isotopic geochemistry, U–Pb and Re–Os geochronology of the Huangganglang Fe–Sn deposit, Inner Mongolia, NE China. Ore Geol. Rev. 59, 109–122.
Zhang, X.Z., Zhang, Z.B., 2003. Geological structure and metallogeny in the southern section of Daxingan'ling, Inner Mongelia. Miner. Resour. Geol. 17, 298–301 (supplement). (in Chinese with English abstract).
Zhang, D.Q., Zhao, Y.M., 1993. Copper Polymetallic Deposits on Great Hinggan Range and its Adjacent Area. Seismological Press House, Beijing, pp. 100–115 (in Chinese).
Zhang, S.H., Zhao, Y., Song, B., Yang, Z.Y., Hu, J.M., Wu, H., 2007. Carboniferous granitic plutons from the northern margin of the North China block: implications for a late Palaeozoic active continental margin. J. Geol. Soc. 164 (2), 451–463.
Zhang, J.H., Ge, W.C., Wu, F.Y., Wilde, S.A., Yang, J.H., Liu, X.M., 2008a. Large-scale Early Cretaceous volcanic events in the northern Great Xing'an Range, northeastern China. Lithos 102, 138–157.
Zhang, L., Zhou, X., Ying, J., Wang, F., Guo, F., Wan, B., Chen, Z., 2008b. Geochemistry and Sr–Nd–Pb–Hf isotopes of Early Cretaceous basalts from the Great Xinggan Range, NE China: implications for their origin and mantle source characteristics. Chem. Geol. 256, 12–23.
Zhang, S.H., Zhao, Y., Song, B., Hu, J.M., Liu, S.W., Yang, Y.H., Chen, F.K., Liu, X.M., Liu, J., 2009a. Contrasting Late Carboniferous and Late Permian–Middle Triassic intrusive suites from the northern margin of the North China craton: geochronology, petrogenesis, and tectonic implications. Geol. Soc. Am. Bull. 121, 181–200.
Zhang, L.C., Wu, H.Y., Wan, B., Chen, Z.G., 2009b. Ages and geodynamic settings of Xilamulun Mo–Cu metallogenic belt in the northern part of the North China Craton. Gondwana Res. 16 (2), 243–254.
Zhang, S.H., Zhao, Y., Song, B., Hu, J.M., Liu, S.W., Yang, Y.H., Chen, F.K., Liu, X.M., Liu, J., 2009c. Contrasting Late Carboniferous and Late Permian–Middle Triassic intrusive suites from the northern margin of the North China craton: geochronology, petrogenesis, and tectonic implications. Geol. Soc. Am. Bull. 121 (1–2), 181–200.
Zhang, S.H., Zhao, Y., Kröner, A., Liu, X.M., Xie, L.W., Chen, F.K., 2009d. Early Permian plutons from the northern North China Block: constraints on continental arc evolution and convergent margin magmatism related to the Central Asian Orogenic Belt. Int. J. Earth Sci. 98 (6), 1441–1467.
Zhang, J.H., Gao, S., Ge, W.C., Wu, F.Y., Yang, J.H., Wilde, S.A., Li, M., 2010a. Geochronology of the Mesozoic volcanic rocks in the Great Xing'an Range, northeastern China: implications for subduction-induced delamination. Chem. Geol. 276, 144–165.
Zhang, L.C., Wu, H.Y., Xiang, P., Zhang, X.J., Chen, Z.G., Wan, B., 2010b. Ore-forming processes and mineralzation of complex tectonic system during the Mesozoic: a case from Xilamulum Cu–Mo metallogenic belt. Acta Petrol. Sin. 26 (5), 1351–1362 (in Chinese with English abstract).
Zhang, Q., Jin, W.J., Li, C.D., Wang, Y.L., 2010c. Revisiting the new classification of granitic rocks based on whole-rock Sr and Yb contents: index. Acta Petrol. Sin. 26 (4), 985–1015 (in Chinese with English abstract).
Zhang, F.Q., Chen, H.L., Yu, X., Dong, C.W., Yang, S.F., Pang, Y.M., Batt, G.E., 2011. Early Cretaceous volcanism in the northern Songliao Basin, NE China, and its geodynamic implication. Gondwana Res. 19, 163–176.
Zhang, K., Nie, F.J., Hou, W.R., Li, C., Liu, Y., 2012a. Re–Os isotopic age dating of molybdenite separates from Hashitu Mo deposit in Linxi County of Inner Mongolia and its geological significance. Mineral Deposits 31, 129–138 (in Chinese with English abstract).
Zhang, X.H., Xue, F.H., Yuan, L.L., Ma, Y.G., Wilde, S.A., 2012b. Late Permian appinite–granite complex from northwestern Liaoning, North China Craton: petrogenesis and tectonic implications. Lithos 155, 201–217.
Zhang, H.F., Zhu, R.X., Santosh, M., Ying, J.F., Su, B.X., Hu, Y., 2013a. Episodic widespread magma underplating beneath the North China Craton in the Phanerozoic: implications for craton destruction. Gondwana Res. 23, 95–107.
Zhang, S.H., Zhao, Y., Davis, G.A., Ye, H., Wu, F., 2013b. Temporal and spatial variations of Mesozoic magmatism and deformation in the North China Craton: implications for lithospheric thinning and decratonization. Earth Sci. Rev. http://dx.doi.org/10.1016/j.earscirev.2013.12.004.
Zhang, W., Jian, P., Kröner, A., Shi, Y.R., 2013c. Magmatic and metamorphic development of an early to mid-Paleozoic continental margin arc in the southernmost Central Asian Orogenic Belt, Inner Mongolia, China. J. Asia Earth Sci. 72, 63–74.
Zhang, X.H., Yuan, L.L., Xue, F.H., Yan, X., Mao, Q., 2014. Early Permian A-type granites from central Inner Mongolia, North China: magmatic tracer of post-collisional tectonics and oceanic crustal recycling. Gondwana Res. http://dx.doi.org/10.1016/j.gr.2014.02.011.
Zhao, Y.M., Zhang, D.Q., 1997. Metallogenic Regularity and Prospective Evaluation of the Copper–Polymetallic Deposits in Daxinganling and Adjacent Areas. Seismological Press House, Beijing (in Chinese).
Zhao, Y.M., Wang, D.W., Zhang, D.Q., 1994. Ore-controlling Factors and Ore-prospecting Models for Copper–Polymetallic Ore Deposits in Southeastern Inner Mongolia. Seismological Press, Beijing (in Chinese).
Zhou, Z.H., Feng, J.R., Lv, L.S., Li, T., Yang, Y.J., 2010a. Ore forming mechanism and the temporal and spatial structure of the Huanggangliang–Wulanhaote tin–lead–zinc–copper–polymetallic metallogenic belt, Inner Mongolia. China Mining Magazine 19, 100–104 (in Chinese with English abstract).
Zhou, Z.H., Lv, L.S., Feng, J.R., Li, C., Li, T., 2010b. Molybdenite Re–Os ages of Huanggang skarn Sn–Fe deposit and their geological significance, Inner Mongolia. Acta Petrol. Sin. 26, 667–679 (in Chinese with English abstract).
Zhou, Z.H., Wang, A.S., Li, T., 2011. Fluid inclusion characteristics and metallogenic mechanism of Huanggang Sn–Fe deposit in Inner Mongolia. Mineral Deposits 30, 867–889 (in Chinese with English abstract).
Zhou, Z.H., Ouyang, H.G., Wu, X.L., Liu, J., Che, H.W., 2014. Geochronology and geochemistry study of the biotite granite from the Baolundaba Cu–W polymetallic deposit in the Inner Mongolia and its geological significance. Acta Petrol. Sin. 30, 79–94 (in Chinese with English abstract).
Zhu, R.X., Chen, L., Wu, F.Y., Liu, J.L., 2011. Timing, scale and mechanism of the destruction of the North China Craton. Sci. China Earth Sci. 54, 789–797.